Retrieval of Microscale Flow Structures from High Resolution Doppler Lidar Data using an Adjoint Model

Tianfeng Chai[1], Ching-Long Lin[1*], Rob K. Newsom[2]

[1] Department of Mechanical and Industrial Engineering and
IIHR-Hydroscience & Engineering
The University of Iowa, Iowa City, Iowa 52242-1527
[2] Cooperative Institute for Research in the Atmosphere, Colorado State University, Fort Collins, Colorado 80523-1375

[*] Corresponding author TEL: 319-335-5673, FAX: 319-335-5669,
E-MAIL: ching-long-lin@uiowa.edu

Abstract

Radial velocity data measured by High Resolution Doppler Lidar (HRDL) are assimilated with a four-dimensional variational data assimilation method (4D-Var), known as an adjoint model, to retrieve microscale flow structures in an atmospheric boundary layer. The control variables of 4D-Var currently consists of initial three-dimensional velocity and temperature fields, as well as profiles of eddy viscosity and thermal diffusivity. The effects of lateral boundary conditions and buffer zones on the retrieval quality are evaluated using identical twin experiments with synthetic observational data prior to HRDL data retrieval. It is found that use of inflow/outflow boundary conditions in conjunction with buffer zones yields good results because buffer zones, which contain no data and separate the domain boundaries from regions having data, act to prevent boundary conditions from affecting retrieval quality. HRDL field observations are then assimilated with 4D-Var, together with the above treatment of boundaries, to recover microscale flow structure in a convective boundary layer. The uncertainty of the retrieved data is assessed by conducting a grid sensitivity test. A large-scale flow structure resembling a dry microburst is observed in the retrieved wind field. Characteristics of this structure are discussed and compared with those of a typical microburst.

1 Introduction

Accurate prediction of weather, climate, and air quality change, requires knowledge about the turbulent processes in the atmospheric boundary layers (ABL). With field measurements acquired using in situ sensors on aircraft, towers, and tethered balloons, or by radar, sonar (SODAR), and lidar remote sensors, the understanding of ABL has been greatly improved. Nevertheless, a genuine picture of the dynamic processes in ABL is far from complete. With advances in computer technology, computational fluid dynamics has played a significant role in studying ABL flows. Although direct numerical simulation of atmospheric flow is still impossible with today's computational power, application of large eddy simulation (LES) to model the ABL has significantly contributed to the current knowledge of the turbulent processes in ABL. For instance, vortical structures and low-speed streaks have been observed in the neutrally stratified ABLs (Moeng and Sullivan 1994, Lin et al. 1996). Convective rolls are seen in the slightly convective ABL (Glendening 1996, Khanna and Brasseur 1998). The strongly convective ABL is now known to be characterized by elongated updrafts (Khanna and Brasseur 1998, Lin 2000). Although LES models are able to generate detailed flow structures in the ABL, they are often limited by idealized lateral and upper boundary conditions, which decouple the interaction between mesoscale (2 km - 2,000 km) and microscale (2 mm - 2 km) atmospheric structures (Jacobson 1999). Near the surface, LES relies on complicated subgrid-scale (SGS) models for physical realization of eddy structures. Some argue that organized coherent structures derived from LES are quite sensitive to SGS models and grid resolution effects.

For field measurements, Doppler radars are widely used and provide amounts of observational data for diagnostic studies of convective systems, severe weather detection, and short-term forecasting, thanks to the NEXRAD (NEXt generation of weather RADar) network deployed in the 1990s. The Doppler radars can provide full volume scan data every 3 to 10 minutes, with 1 km^2 horizontal resolution, 500 m vertical resolution, and velocity accuracy of 0.5 to 1.0 m s^{-1}. Researchers wishing to develop and verify improved theories and models for turbulent processes in ABL often demand measurements that exceed the capability of the Doppler radars. To meet their needs, different lidar systems have been developed over the past 20 years. For instance, the 248-nm water Raman lidar (Eichinger et al. 1994) has a 3 m range resolution, which is better than the grid resolutions used in most ABL flow simulations. This lidar has detected Rayleigh-Bernard-like, "dumbbell" shaped coherent structures of 10

to 20 m in diameter in the lower surface of the equatorial marine boundary layer (Cooper et al. 1997). Another recently developed instrument is the High Resolution Doppler Lidar (HRDL), (Grund et al. 2001, Wulfmeyer et al. 2000). Designed and developed at the National Oceanic and Atmospheric Administration (NOAA) Environment Technology Laboratory (ETL), HRDL is a solid state coherent Doppler lidar that operates at a wavelength of 2 μm, with 30 m range resolution and is capable of 10 cm s^{-1} velocity measurement precision. HRDL has demonstrated its effectiveness at detecting coherent structures in the ABL in numerous field campaigns since its first successful deployment during the Lasers in Flat Terrain (LIFT) experiment in 1996. Weckwerth et al. (1997) presented the first observation of linearly organized coherent structures in the ABL surface layer using HRDL data. Linear streaks with horizontal spacing of about 200 m are clearly recognizable from HRDL radial velocity contour plots.

Nevertheless, the analysis of lidar data is quite limited at present. In published works, radial velocity and reflectivity fields are often presented to show the presence of coherent structures or other phenomena without considering cross-beam velocity components. Although some structures are distinguishable from displays of Plan Position Indicator (PPI) or Range Height Indicator (RHI), they are incomplete and might be misleading. Deploying multiple lidars clears up the ambiguity, but it is impractical in the near future. The limited information obtained by lidar must be assimilated into an LES model to derive complete, detailed ABL wind and temperature fields.

The four-dimensional variational data assimilation method (4D-Var) has been successfully implemented using Doppler radar measurements. It proves to be able to retrieve atmospheric flow fields at mesoscale more accurately than the traditional technique (Sun et al. 1996). In the 4D-Var application, radial velocity and reflectivity data observed by radar systems are assimilated into a numerical model through minimization of the squared difference between field observations and model predictions. Besides retrieving the detailed flow structures, similar techniques have demonstrated the ability to infer other variables, such as chemical species of O_3, NO_2, and O_2 (Daescu et al. 2000) and total column water-vapor amount (Gerard et al. 1999).

The objective of the work is to apply the 4D-Var to HRDL radial velocity data to recover complete wind and temperature fields for microscale atmospheric structure studies. Issues concerning boundary conditions and retrieved data quality will be addressed. From the retrieved data sets, microscale atmospheric structures are examined, demonstrating 4D-Var

capabilities in the study of the ABL. The 4D-Var technique used was developed for mesoscale Doppler radar observation (Sun et al. 1998) and later modified to deal with microscale ABL flows (Lin et al. 2001, 2002, Chai et al. 2002). Before applying the 4D-Var to HRDL data, identical twin experiments (ITEs) are conducted. In these ITEs, the scan volume of synthetic radial velocity data is constructed to mimic a realistic scan volume which has available data only within certain ranges of elevation and azimuth angles. The idealized boundary condition employed in the ITEs of Lin et al. (2001) becomes impractical in HRDL data retrieval. The ITEs in this work are used to assess the effects of Dirichlet and inflow/outflow boundary conditions that can be easily implemented in HRDL data retrieval. Buffer regions enclosing the scan volume work effectively with the foregoing two boundary conditions. Finally, HRDL observations are assimilated using the 4D-Var that also treats eddy viscosity and thermal diffusivity profiles as control variables (Chai et al. 2002). A flow structure resembling a dry microburst is identified from the retrieved wind field, and its characteristics are discussed.

The paper is organized as follows. Section 2 briefly describes the numerical formulations of the present 4D-Var, including the prediction model, the adjoint equations, and the optimization method. Section 3 presents the results of the ITEs to assess boundary condition and buffer zone effects. Section 4 discusses HRDL radial velocity data retrieval. Section 5 summarizes results and draws conclusions.

2 Numerical Method

The current 4D-Var system (Lin et al. 2001, 2002, Chai et al. 2002) has several features for microscale turbulent structure retrieval. In addition to the initial wind and temperature fields, eddy viscosity and thermal diffusivity model parameters are treated as control variables. All control variables are updated iteratively to minimize the cost function, which measures the difference between model predictions and field observations. A set of adjoint equations constructed via variational analysis calculates the cost function gradients with respect to control variables.

2.1 Prediction model

The prediction model for dry air solves incompressible Navier-Stokes equations with Boussinesq approximation subject to a pre-specified vertical mean temperature profile.

$$\nabla \cdot \mathbf{U} = 0, \tag{1}$$

$$\frac{\partial \mathbf{U}}{\partial t} + \mathbf{U} \cdot \nabla \mathbf{U} = -\frac{1}{\rho_\circ} \nabla P + \mathbf{G} \frac{\theta}{\Theta_\circ} + \nabla \cdot (\nu(z) \nabla \mathbf{U}), \tag{2}$$

$$\frac{\partial \theta}{\partial t} + \mathbf{U} \cdot \nabla (\theta + \Theta) = \nabla \cdot (\kappa(z) \nabla (\theta + \Theta)), \tag{3}$$

where velocity vector $\mathbf{U}$ has three components U_1, U_2, and U_3 (U, V and W) in x_1, x_2, and x_3 (x, y, and z) directions respectively. Spatial variables x_1 and x_2 correspond to the two horizontal directions and x_3 is the vertical direction. $\mathbf{G} = (0,\ 0,\ -g)$ and g is the gravitational acceleration. $\rho_\circ$ is the reference density. θ, Θ, and $\Theta_\circ$ are fluctuating, background (function of z only), and reference virtual potential temperature, respectively. Lowercase variables denote fluctuating parts of variables. Eddy viscosity $\nu(z)$ and thermal diffusivity $\kappa(z)$ are assumed functions of height only. Dependent variables are arranged on a staggered, orthogonal grid. A second-order finite volume method is applied for spatial differencing. The second-order Adam-Bashforth method is used for time-advancement of dependent variables. Mass conservation is enforced by solving a pressure-Poisson equation derived from the continuity equation (1) and the momentum equations (2).

To apply this model for flow structure retrieval in a convective boundary layer (CBL), a surface momentum and temperature flux model is implemented to enforce satisfaction of the Monin-Obukhov similarity theory at the first vertical grid level immediately above the surface (Lin et al. 2001). The gradient-free boundary condition is imposed at the domain top for U, V, and θ, whereas the Dirichlet boundary condition $W = 0$ is used for W. Two lateral boundary conditions are evaluated in section 3. Features such as Coriolis force and Galilean transformation of the coordinates with a constant speed, are added to the model. The Galilean transformation mimics a moving grid. It is implemented to reduce the maximum velocity of the entire field, which subsequently relaxes the stability constraint permiting large time steps.

2.2 Optimization method

To reduce the difference between model predictions and field observations, an optimization procedure is performed to update the unknown control variables. In data assimilation, control variables typically include the primary variables at the initial state. Model parameters of eddy viscosity and thermal diffusivity are added as control variables when dealing with

real lidar data, where these parameters are difficult to approximate. Numerically, the cost function is defined as

$$J = \sum_{t} \sum_{x,y,z} \left[\alpha \left(U_{rad} - U_{rad}^{obs} \right)^2 \right] + \sum_{x,y,z} \left[\beta (\nabla \cdot \mathbf{U})^2 \right]_{t=0} \tag{4}$$

where U_{rad} and U_{rad}^{obs} are radial velocities obtained from the prediction model and field observation, respectively. $\sum_t$ and $\sum_{x,y,z}$ denote summations over time and space, respectively. α is a validity coefficient indicative of the quality of the observation data. In the current study, it is taken as unity for good observations and zero for bad ones. The second term, which is a penalty term, represents non-divergent constraint for the initial velocity field. Given that this penalty term does not dominate the cost function, the value for coefficient β should be as large as possible to obtain a divergence-free initial velocity vector field. We chose $\beta = 100$ as suggested in Lin et al. (2001). The relationship between the radial velocity and the velocity vector is

$$U_{rad} = \frac{\mathbf{U} \cdot (\mathbf{r} - \mathbf{r}_\circ)}{|\mathbf{r} - \mathbf{r}_\circ|} \tag{5}$$

where vector $\mathbf{r_0} = (x_{1\circ},\ x_{2\circ},\ x_{3\circ})$ denotes the lidar location and $\mathbf{r}$ represents the space coordinates of a data point.

The adjoint model is adopted to calculate cost function gradients with respect to all control variables. This involves converting the constrained minimization problem into an unconstrained problem through the Lagrange multiplier. That is, the constraints [Eqs. (2) and (3), and the pressure-Poisson equation derived from Eqs. (1) and (2)] multiplied by Lagrange multipliers ($\lambda_{\mathcal{F}}$, also known as adjoint variables) are appended to the cost function (4). It leads to

$$L = J + \sum_{\mathcal{F}} \sum_{t} \sum_{x,y,z} \lambda_{\mathcal{F}} (LHS_{\mathcal{F}} - RHS_{\mathcal{F}}), \tag{6}$$

where $\mathcal{F}$ represents any of variables U, V, W, θ, and P. $LHS_{\mathcal{F}}$ and $RHS_{\mathcal{F}}$ are the "left hand side" and "right hand side" of the "$\mathcal{F}$ equation", which is one of the aforementioned governing equations. The unconstrained minimization of L with respect to U, V, W, θ, P, λ_U, λ_V, λ_W, λ_θ, λ_P, ν, and κ is equivalent to the constrained minimization of J with respect to U, V, W, θ, P, ν, and κ. The first variations of L with respect to λ_U, λ_V, λ_W, λ_θ, and λ_P recover the governing equations. Those with respect to U, V, W, θ, and P generate adjoint equations for $\lambda_{\mathcal{F}}$. The backward integration of the adjoint equations yields λ_U, λ_V,

λ_W, and λ_θ at initial state. These correspond to the gradients for initial U, V, W, and θ fields, respectively. That is,

$$\frac{\partial L}{\partial \mathcal{F}(x,y,z,t=0)} = -\lambda_{\mathcal{F}}(x,y,z,t=0). \tag{7}$$

The gradients with respect to $\nu(z)$ and $\kappa(z)$ are

$$\frac{\partial L}{\partial \nu(z)} = \sum_{\mathcal{F}=U,V,W} \sum_t \sum_{x,y} (\nabla \lambda_{\mathcal{F}} \cdot \nabla \mathcal{F}), \tag{8}$$

$$\frac{\partial L}{\partial \kappa(z)} = \sum_t \sum_{x,y} (\nabla \lambda_\theta \cdot \nabla \theta). \tag{9}$$

With the above gradients, the limited memory BFGS (L-BFGS) method (Liu et al. 1989) is applied to find the optimal initial guess and parameters $\nu(z)$ and $\kappa(z)$ for the prediction model, whose solution best fits the observations in a least squares sense. It is noted that solving the nonlinear problem requires many iterations of L-BFGS updating of control variables to meet a certain criterion. Each iteration performs a forward integration of the prediction model, a backward integration of the adjoint model, and an optimization of the initial guess.

2.3 Smoothness penalty functions

Long and Thacker (1989) demonstrate that the use of a spatial smoothness constraint for data assimilation into an equatorial ocean model improved the accuracy of the retrieved data. Sun et al. (1991) and Sun and Crook (1996) also illustrate that temporal and spatial smoothness constraints provide supplemental information on the retrieved variables and accordingly helpe yielding better solutions. The effect of these penalty functions becomes more pronounced for variables whose information is lacking or whose observations contain substantial errors.

In this paper, the spatial smoothness constraint appended to the cost function reads

$$P_s = \sum_{\mathcal{F}=U,V,W,\theta} \sum_t \sum_{x,y,z} \left[\zeta_{\mathcal{F}} \left(\frac{\partial^2 \mathcal{F}}{\partial x^2} + \frac{\partial^2 \mathcal{F}}{\partial y^2} + \frac{\partial^2 \mathcal{F}}{\partial z^2} \right)^2 \right]. \tag{10}$$

In all the past practice, determination of the penalty coefficients $\zeta_{\mathcal{F}}$ is empirical. A basic requirement is that the penalty terms shall be large enough to be effective, but shall not dominate the cost function. Rather than choosing the values of the coefficients $\zeta_{\mathcal{F}}$ by trial and error, a dynamic procedure (Lin et al. 2002) is employed to control the contribution of the smoothness term by each variable to be 5% or less of the total cost function.

3 HRDL Observational Data

The HRDL observational data were obtained during the CASES-99 (Cooperative Atmospheric Surface Exchange Study - 1999) field experiment near Leon, Kansas. The data set was collected from 19:23:57 to 19:53:19 UTC (Universal Time Coordinate) on October 24, 1999. It was in a typical convective afternoon, when the local Central Daylight Time (CDT) was from 14:23:57 to 14:53:19 CDT. The platform of the lidar location was at latitude 37.6360° and longitude −96.7339°. The observational data were processed with 90 m range gates and 100 pulse averages, with the pulse repetition frequency as 200 Hz. Due to two-times over-sampling in time and three-times over-sampling in range, the data indicate a 0.25 second time resolution and 30 mrange gates.

The observational data include 19 scan volumes, which are made up of a sequence of plan position indicator (PPI) scans. There are 10 PPI sectors in each scan volume, with elevation angles ranging from 1° to 19°. The PPI sectors are spanned from azimuth angle −30° to 30°, centered to the north. In each sector, light beams are about 2° apart, with 198 range gates in each beam. It is very unlikely to get the same azimuth angles in different sector scans. During operation, actual elevation and azimuth angles, along with other parameters, such as the observational time associated with light beams, were recorded in the original radial velocity data. The radial velocity data were post-processed with quality control, removing radial velocities associated with suspected hard target returns and low signals. Radial velocity contours in scan planes with elevation angles of 1° and 19° are shown in Fig. 1. Although the biggest range for the scan is about 6 km, only the ranges less than or equal to 3 km are shown here since there are almost no valid data beyond 2.5 km range. Blank spots in the scan planes represent the bad observations. The displayed volume is the 15th in the 30 minutes period, denoted as VOL15 in the following text. From this volume data, a high radial velocity region, outlined by iso-surface $U_{rad}^{obs} = 5$ m s^{-1} in Fig. 1, can be easily identified. Figure 2 displays a time sequence of slices at 5° elevation angle, from scan volumes VOL13 to VOL17, suggesting that a high-speed structure moved through the scanned region. Lack of the cross-beam velocity components makes it difficult to infer additional information without further analysis. HRDL takes about about 90 seconds to sweep one volume of data. The time variation between any two beams in a single volume must be taken into account in data assimilation.

4 Boundary Conditions and Buffer Zones

Performing ITEs allows study of boundary conditions and buffer zones effects on retrieved results. To emulate lidar scan features, range constraints on elevation and azimuth angles are imposed on the synthetic observational data. Buffer zones, the regions between the domain boundaries and the lidar scan volume, contain no data.

4.1 Synthetic observational data

A computational domain of $5 \times 5 \times 1.875$ km^3 with a uniform grid of $NX \times NY \times NZ = 48 \times 48 \times 45$ is used for most cases. A smaller domain of $3.333 \times 3.333 \times 1.875$ km^3, with grid size $32 \times 32 \times 45$, is applied to study computational domain effects. A geostrophic wind of 10 m s^{-1} and a surface temperature flux of 0.24 K m s^{-1} (K, Kelvin temperature scale) are assumed, driving the simulated CBL flow. At $z = 980$ m, a capping inversion layer is imposed. The roughness height $z_\circ$ is 0.16 m. Coriolis parameter f is 10^{-4} s^{-1}. Stability parameter $-z_i/L$ is about 15, where z_i is the averaged CBL height and L is the Monin-Obukhov length.

Integrating the prediction model (1)-(3) forward in time, synthetic observation data are generated. Initial conditions used for synthetic data generation are obtained by running the NCAR-Large-Eddy-Simulation (NCAR-LES) code (Moeng 1984, Sullivan it et al. 1994). Simulated turbulence flow develops and evolves over a physical time period of 1.56 hours. NCAR-LES provides prediction model initial conditions for velocity and temperature fields, as well as profiles of eddy viscosity and thermal diffusivity. To generate synthetic observations, a 5 second time step is used in integrating the prediction model for 50 seconds before recording 3D data every 25 seconds for 300 seconds. The mean and variance profiles of the simulated velocity fields are displayed in Figs. 3(a) and 3(b). The CBL is capped by an inversion layer, where temperature increases with height. It is found that the simulated data agree reasonably well with field data (Lenschow et al. 1980).

Recorded 3D flow fields permit calculation of radial velocities using Eq. (5). In Fig. 4, the lidar is assumed at (0, 0, 0) m. For the current HRDL data set, each volume scan spans about 90 seconds. To emulate the scan pattern in a simple manner, several $x - y$ planes of data are assumed to be acquired every 25 seconds. A total of 3 volumes of data are available in a period of 300 seconds. The positive x direction is chosen as the zero azimuth angle. The azimuth angle of scan volumes varies from 15° to 75°. The maximum elevation angle is set

at 20°. There is no restriction on the range in the radial direction because the radial range of the HRDL is large enough to cover the computational domain. The synthetic observational data are constructed, discarding the data outside the constraints.

Radial velocity observations for ITEs are generated from the available 3D instantaneous flow fields, making it easy to assess the quality of the retrieved flow fields by comparison with the original exact flow fields. Linear correlation coefficients and root-mean-square (RMS) errors are calculated to quantify the differences between the retrieved and exact fields. The correlation coefficient $\sigma_{\mathcal{F}}$ is defined as

$$\sigma_{\mathcal{F}} = \frac{\overline{\mathcal{F}' \cdot \mathcal{F}'_{\circ}}}{\sqrt{\overline{\mathcal{F}'^2}} \cdot \sqrt{\overline{\mathcal{F}'^2_{\circ}}}}, \tag{11}$$

where $\mathcal{F}'$ designates any retrieved fluctuating velocity component or temperature, and $\mathcal{F}'_{\circ}$ represents its exact counterpart. The overline denotes spatial averaging over an $x-y$ plane. In calculating correlation coefficient $\sigma_{\mathcal{F}}$ or RMS error $\epsilon_{\mathcal{F}}$ in a $x-y$ plane, only the scanned region is considered. $\epsilon_{\mathcal{F}}$ and $\sigma_{\mathcal{F}}$ can be computed at every vertical level and instant due to the availability of exact flow fields. Observational data are located mostly in the lower region. Correlation coefficients and RMS errors are calculated for $z < 400$ m only. Results at the middle of the assimilation time window are more accurate than those at the beginning or end (Lin et al. 2001). The results presented subsequently are taken from the middle of the assimilation time window.

4.2 Boundary conditions

Two lateral boundary conditions are considered, Dirichlet boundary conditions and inflow/outflow boundary conditions. For Dirichlet boundary conditions, mean vertical profiles of U, V, and θ are estimated and assigned to lateral boundary nodes. For inflow/outflow boundary conditions, velocity solutions from the previous iteration are used to determine inflow/outflow conditions. If the velocity vector points into the computational domain, i.e. the inflow boundary, dependent variables are specified with available mean profiles. Otherwise, if the velocity points outside, i.e. the outflow boundary, gradient-free Neumann conditions are applied to the U, V, and θ variables. For all ITEs, W values are set to zero at the boundary nodes. Global mass conservation is enforced for each iteration by uniformly distributing a mass residual on lateral boundary nodes.

The ITEs conducted are described in table 1. Correlation coefficients and RMS errors are summarized in table 2. Using the sector-like scan volume as a reference, there are various

ways of selecting the computational domain for 4D-Var retrieval. Figure 4 illustrates two choices. One domain is made big enough to cover all volume data to utilize all available information. The other domain is smaller, at $3.333 \times 3.333 \times 1.875$ km^3 with a grid of $32 \times 32 \times 45$, based on the assumption that a high ratio of data to grid size may improve retrieval quality. The aforementioned boundary conditions are applied to the two domains for comparison.

Table 1 shows that only cases IT3 and IT4 use the small computational domain. With Dirichlet boundary conditions applied, case IT1, having a big domain, produces better results than case IT3 (table 2). The RMS error of velocity components for case IT1 is about 0.1 m s^{-1} smaller than for case IT3. Case IT1 yields better retrieved temperature data. The RMS temperature error for case IT1 is 0.061 K smaller than that for case IT3. The correlation coefficients for case IT1 are all greater than those for case IT3. Comparison between cases IT2 and IT4, which implement inflow/outflow boundary conditions, shows consistently that big domain case IT2 yields significantly better retrieval than small domain case IT4. These ITEs suggest that lateral boundary condition treatment has only minor effect on retrieval, as indicted by both correlation coefficients and RMS errors. Inflow/outflow boundary conditions are slightly better than Dirichlet boundary conditions. Implementation of Dirichlet boundary conditions, however, is much easier. The reason why the big domain produces better retrieval can be explained by the concept of buffer zones that will be discussed next.

4.3 Buffer zones

The buffer zone concept is found in oceanic data assimilation literature. Gavart et al. (1999) implemented a special boundary treatment in the assimilation of satellite altimeter data into a primitive-equation ocean model. A surrounding recirculating area was added to separate the interior. The added surrounding regions were referred to as buffer zones. Ezer et al. (2000) applied the same concept in their sensitivity studies of the Princeton Ocean Model, with temperature and salinity fields relaxed in buffer zones near the boundaries. The application of buffer zones to 4D-Var retrieval is the focus of this section.

For big domain cases IT1 and IT3, only 26% of the region increased over the small domain contains radial velocity data. The data, however, may not effectively improve retrieval quality. It is speculated that the added blank region, which contains no data, acts as a buffer which blocks inaccurate boundary conditions from affecting the inner region containing data. To clarify this conjecture, case IT5 is conducted. This case is almost the same as IT1 except

that constraints on elevation and azimuth angles are removed so that the amount of data nearly double. With more observational data, case IT5 should yield better results than IT1 if the "buffer zone" concept is invalid. The results, however, show that case IT5 has worse retrieval, indicated by RMS errors and correlation coefficients for variables U, V, and θ. Although the RMS error of the retrieved W velocity for case IT5 is 0.008 m s^{-1} smaller than that of IT1, it is insignificant compared with the U and V components. Use of buffer zones in 4D-Var improves retrieval quality by preventing inaccurate boundary conditions from contaminating the inner region.

Another set of identical twin experiments shed yet more light on buffer zone effects. In these ITEs, the scan volumes are centered columns surrounded by buffer zones of the same width on all four sides. Buffer zone size can be measured easily by counting vertical grid planes parallel to lateral boundaries. Six cases with buffer zones up to 16 grid planes to a side are examined. The convergence criterion for these ITEs is

$$\sqrt{\frac{\sum_1^N \xi_{\mathbf{i}}^{\mathbf{2}}}{N}}_{NTER} \leq 0.01 \sqrt{\frac{\sum_1^N \xi_{\mathbf{i}}^{\mathbf{2}}}{N}}_{NTER=0}, \tag{12}$$

where N is the number of control variables. NTER is number of iterations, and $\xi_{\mathbf{i}}$ is the cost function gradient with respect to the ith control variable. Figure 5 illustrates buffer zone size effect on retrieval. The number of iterations required to meet the termination criterion, the normalized cost function, the RMS errors, and the correlation coefficients of these cases are plotted versus buffer zone size. Results show that solutions are reached faster with buffer zones introduced. An optimal size for retrieval is indicated by variations of the cost function, the RMS errors, and the correlation coefficients. Buffer zones with two vertical grid planes on each sideare most effective in retrieval of the "centered-column" volume data. For sector-shaped lidar scan volume, it is difficult to determine optimal buffer size. Volume shape depends on elevation and azimuth angle parameters. Different lidar scan schemes reflect different constraints on the angles and the range. The above experiments demonstrate that a big model domain covering sector-shaped HRDL data can be used in real lidar data retrieval.

4.4 Observational errors

In contrast with the radial velocity provided for the previous ITEs, real lidar observations always contain errors. Lin et al. (2001) conducted sensitivity tests on observational errors of various amplitude and spatial correlation. For the introduction of the buffer zones, this issue

must be re-examined. As quality control is routinely applied in post-processing, errors are not severe in HRDL observational data. For conditions typically encountered in the ABL, the radial velocity measurement precision can be as high as 0.1 m s^{-1}. To simulate actual lidar observation errors, uniformly distributed random errors are added to observations used in cases IT1 and IT2, which apply different boundary conditions. The error amplitudes added to case IT1 are chosen as 20% of radial velocities. The case is listed as IT6 in tables 1 and 2. Case IT7 is modified from case IT2 by adding random errors in the range of -0.1 to 0.1 m s^{-1}. Comparison of the results between cases IT6 and IT1 shows that the retrieved flow fields are only slightly affected. Increases of the RMS errors ϵ_U and ϵ_V by 0.018 m s^{-1} and 0.010 m s^{-1}, respectively, are observed after introducing the random errors. The difference is negligible. Comparison between cases IT7 and IT2 shows consistently that observational errors only slightly affect the solution if not negligible. These results demonstrate that the 4D-Var method is insensitive to the presence of small random observational errors.

4.5 Retrieved flow structures

In this section, a detailed inspection of retrieved flow structures is presented. In table 2, case IT2 produces the best retrieval. Vertical distributions of the correlation coefficients and the RMS errors of this case are displayed in Fig. 6. Since the number of radial velocity data decreases with height, the retrieval quality deteriorates with height too, having larger RMS errors and smaller correlations. Figure 7 displays the retrieved instantaneous flow field at $t = 150$ s in the horizontal plane $z = 229$ m and the corresponding flow field used to generate observations. The mean value calculated at that level has been deducted from the total in order to show the flow pattern clearly. There are discrepancies in the small scale flow structures, but the larger scale flow structures agree well. The magnitudes of the retrieved fluctuating components are in general smaller than those of the original flow field used for synthetic observation generation. This may be attributed to the smoothness constraint that removes the effect of high-spatial-frequency observational errors. In the next section, buffer zones and the inflow/outflow boundary conditions are applied to 4D-Var data assimilation of HRDL observations.

5 HRDL Data Retrieval

5.1 Computational grid

A computational domain $2400 \times 2400 \times 1250$ m^3 is employed in the assimilation of HRDL observations. Except in one case to test grid sensitivity, all other cases use a grid $NX \times NY \times NZ = 48 \times 48 \times 25$. Axes x, y, and z direct to the north, west, and upward, respectively. The coordinates of the HRDL location is $(0, 0, 25)$ m. Figure 1 shows that the chosen computational domain covering most of the scan volume. Buffer zones are located between the lateral boundaries and the region containing data.

Since HRDL observations are recorded in the spherical coordinate system, they are mapped to the Cartesian computational grid. The grid resolutions for the data are 2° in elevation and azimuth angles, and 30 m in the radial direction. For any computational grid point c inside the scan volume, the radial velocity and its correspondent observational time are calculated by weighted averaging of data at the 8 vertices of the spherical grid element that enclose point c.

$$U_{rad}^{obs(c)} = \frac{\sum_{i=1}^{8} \frac{1}{d^{(i)}} U_{rad}^{obs(i)}}{\sum_{i=1}^{8} \frac{1}{d^{(i)}}}, \tag{13}$$

$$t_{obs}^{(c)} = \frac{\sum_{i=1}^{8} \frac{1}{d^{(i)}} t_{obs}^{(i)}}{\sum_{i=1}^{8} \frac{1}{d^{(i)}}}, \tag{14}$$

where $d^{(i)}$ is the distance between vertex i and point c. Bad observational data as determined by the lidar quality control algorithm are excluded from averaging. If all 8 vertices are "bad", $U_{rad}^{obs(c)}$ is specified a very large number signifying a void point in the scan volume. Since the data observational time in a single scan volume can vary by up to 90 seconds, time information must be provided to the 4D-Var model for assigning each data point an appropriate observational time within a resolution of 2 seconds.

5.2 Input data and mean profiles

There are a tremendous amount of data taken during the CASES-99 field experiment. The sounding data of pressure, air temperature, and dew point temperature taken from 19:08:51 UTC ($z = 0$ m) to 19:14:33 UTC ($z = 1250$ m) on the same day are provided at CASES-99 web site (www.joss.ucar.edu/cases99/). They are used to find the virtual potential temperature profile by converting moist air into dry air at the standard pressure of 10^5 Pa. The

resulting profile is shown in Fig. 8. The height of the mixing layer is about 700 m. Mean velocity profiles, used in inflow/outflow boundary conditions, are approximated using "bin method" (Banta et al. 2002), where the scan volumes are uniformly divided along the vertical. Each division (bin) of data at a given height is processed independently to obtain mean velocities of U_b and V_b for that bin. Assuming zero mean vertical velocity, U_b and V_b can be obtained through an optimization procedure. The cost function of each bin is defined as

$$L = \sum_j (U_b \cos\gamma_j \cos\phi_j + V_b \cos\gamma_j \sin\phi_j - U_{rad_j})^2, \tag{15}$$

where γ is the elevation angle, ϕ is the azimuth angle, and U_{rad} is the measured radial velocity. The running index, j, represents each of the observations in a given bin. Minimization of the cost function (15) by solving $\partial L/\partial U_b = 0$ and $\partial L/\partial V_b = 0$ gives the values of U_b and V_b for the bin. Figure 9 shows wind profiles approximated with two division heights, i.e. $dz = 10$ m and $dz = 50$ m, using all 19 scan volume data sets. The results are consistent although the profile using a small $dz = 10$ m is not smooth due to the decrease of data in each bin. These "bin" mean profiles vary slightly, but are found to have little effect on retrieval if buffer zones are applied. For the following assimilations, the mean velocity profile approximated with $dz = 50$ m using VOL13-VOL17 data is applied to specify inflow/outflow boundary conditions. The mean velocities above a capping inversion layer ($z \geq 750$ m), where data are scarce, are specified as $U_b = 6.7$ m s^{-1} and $V_b = 0.0$ m s^{-1}. The surface temperature 298.0 K, the net radiation temperature flux 0.25 K m s^{-1}, and the friction velocity 0.35 m s^{-1}, from the CASES-99 web site, are provided to the 4D-Var model to specify surface boundary conditions.

As shown in Fig. 2, a flow structure characterized by high radial velocity moved through the scanned region during VOL13-VOL17. Four 4D-Var experiments are conducted based on the five volumes of data to study this structure. The simulation time window for each case is 180 seconds, which covers 2 volume scans. Lin et al. (2001) show that two volumes of data are needed for 4D-Var. Each case thus assimilates two volumes of data. For instance, case AC1 uses observations VOL13 and VOL14 as inputs, and case AC2 uses VOL14 and VOL15, etc. as shown in table 3.

5.3 Radial velocity misfit

Without the exact flow field for comparison as in ITEs, only radial velocity data can be used to assess retrieval. Using retrieved flow fields, the correspondent radial velocity field can be

reconstructed according to lidar location and scan scheme. With the reconstructed radial velocity data, called "would-be" observations hereafter, the RMS of radial velocity misfit Δ can be calculated.

$$\Delta = \sqrt{\overline{(U_{rad} - U_{rad}^{obs})^2}}, \tag{16}$$

where U_{rad} denotes would-be radial velocity and U_{rad}^{obs} is HRDL radial velocity. The overline denotes the average over all data. Figure 10 shows the decrease of misfit Δ with iteration. Δ is reduced from 1.59 m s^{-1} to 0.59 m s^{-1} in the first 10 iterations. The convergence speed slows down eventually. From iteration 100 to 200, Δ only reduces from 0.178 m s^{-1} to 0.131 m s^{-1}. The termination criterion shown below is set for all the cases in this section.

$$\Delta \leq 0.2 \text{ m s}^{-1}. \tag{17}$$

Table 3 lists the iteration numbers conducted for each case to meet (17). Figure 11 shows contour plots of would-be radial velocities reconstructed from the AC2 retrieval results and corresponding HRDL observations. In Fig. 11 (a), flooded contour levels are based on average cell values of VOL15 radial velocities at elevation angle 5°. Blank regions in the figure represent bad observations. Figure 11 (b) shows contours of would-be radial velocities which fill most of blank regions in Fig. 11 (a). As VOL14 provides valid observations at void regions of VOL15, some blank regions are filled through 4D-Var with credible would-be radial velocities. Blank regions in Fig. 11 (b) correspond to the grid points which have no U_{rad}^{obs} data in VOL14 or VOL15. The two contour plots agree well in general. Differences in small-scale features are attributed to the termination criterion (17), $\Delta \approx 0.2$ m s^{-1}, and are quantified below.

Figure 12 shows the probability density function (PDF) of radial velocity misfits for case AC2. The PDF is constructed using an interval of 0.01 m s^{-1} with 33422 observations. Distribution is nearly symmetrical with respect to $U_{rad} - U_{rad}^{obs} = 0$. The arithmetic mean of the misfit is 3.3×10^{-5} m s^{-1}. The standard deviation of misfit is 0.2 m s^{-1}, consistent with the specified termination criterion. A normal distribution function based on the same mean and standard deviation is plotted for comparison. The actual distribution has a higher probability of occurrence at smaller misfits than the normal distribution. This implies good compatibility of retrieved wind data with actual lidar observations.

5.4 Grid resolution

Use of a fine grid is expected to generate more detailed information, but it is prohibitive in practice due to intensive computation and memory demands. The previous HRDL data assimilation would require 4 Gigabytes of computer memory if the space resolution is doubled in each dimension. ABL flow usually varies more in the vertical direction than in the horizontal directions, so case AC5 with $NZ = 50$ that doubles the vertical grid resolution of previous cases is performed to evaluate the retrieval sensitivity to grid resolution.

Figure 13 shows eddy viscosity profiles retrieved from cases AC3 and AC5. The two profiles have similar shapes. The one with lower resolution, case AC3 with $NZ = 25$, results in larger eddy viscosities. Since sub-grid Reynolds stresses are approximated by eddy viscosities, a low resolution case containing more sub-grid turbulence energy is expected to generate large eddy viscosities. This explains the difference in the two profiles. Local maxima locations from the two profiles suggest that turbulent motions are the strongest near the ground ($z \sim 50$ m). There exists another strong turbulent region close to the capping layer, where $z \sim 600$ m.

Retrieved velocity fluctuations of cases AC3 and AC5 are displayed in Fig. 14. Most large-scale flow features captured are the same in both cases. There are some differences in small-scale flow structures. To identify the source of the differences, the 3D velocity vectors of case AC3 are subtracted from those of case AC5. This requires interpolation of AC3 data into the fine mesh of AC5. Absolute differences in U, V, and W components averaged throughout the domain are 0.29, 0.52, and 0.65 m s^{-1}, respectively. Figure 15 shows difference vectors in horizontal and vertical planes. The main differences are in cross-beam direction, normal to the radial-beam direction of lidar, due to the lack of tangential direction data. To quantify the differences, RMS values of vectors in Figs. 15(a) and 15(b) in radial and tangential directions are computed. They are 0.16 and 0.83 m s^{-1} (radial and tangential directions) in Fig. 15(a), and are 0.23 and 0.69 m s^{-1} in Fig. 15(b).

Figure 16 displays the PDF distribution of observations and RMS magnitudes of the above difference vectors as a function of radial distance (range) from the lidar. The PDF distribution of observations indicates data frequency, showing HRDL data becoming scarce at very small and large distances, as expected. Maximum PDF occurs at around the range of 1400 m. Data frequency obviously correlates with the RMS of differences between fine and coarse grid solutions, as shown in the figure. Large differences occur when data are lacking. The corollary is also true. Retrieved data from the central region of the model domain are

most accurate.

5.5 Instantaneous flow structures

HRDL scan volume is composed of radial velocity along light beams in the radial direction at different instants. The 4D-Var fills in variables that the HRDL cannot sense, throughout time and space, and integrates different variables consistently to develop missing information. Recovered 3D instantaneous velocity vectors make it possible to study microscale atmospheric structures which are difficult to model and observe.

Figures 17 and 18 display horizontal and vertical slices of 3D flow fields developing from VOL13 to VOL17. These are taken from cases AC1-AC4 retrieved results (table 3) at the middle of the assimilation time window. In Fig. 17, velocity fluctuations in a horizontal plane at $z = 175$ m are displayed. Radial velocity $U_{rad} = 4.0$ m s^{-1} contours denoted by bold dot-dashed lines are superimposed on vector fields to identify high-speed structures. A high-speed structure is seen coming from the left (south) in Fig. 17(a). Another is found near the upper right corner. Recovered velocity fluctuations are consistent with these contour lines. In subsequent frames (Figs. 17(b)-17(d)), the structure on the left progresses toward the north and veers slightly to the west, finally merging with the structure on the right becoming a big structure. Tracing a region marked by a solid circle in Figs. 17(a)-17(c), the front of the high-speed structure moves at about 6 m s^{-1}.

Figure 18 displays fluctuating velocity vectors in a vertical plane at $y = 0$ m, corresponding to the event identified in Fig. 17. This reveals horizontally aligned vortical (roll) structures, denoted by solid lines with arrows, progressing from the left to the right (Figs. 18(a)-18(d)). Pressure fluctuation contours are superimposed to illustrate the downdraft and locate the outflow front in the vertical planes. Comparison with the locations of vortices suggests that vortices are formed ahead of and above the moving front. These vortices cause strong updrafts and undulation aloft, indicated by the dashed lines in Fig. 18. In theory, the downdraft should be physically associated with low-temperature heavy air. The recovered temperature field is examined in Fig. 19. The low-temperature region coincides with the downdraft, which pushes the high-temperature region to the right (north). The highest temperature fluctuations occur around $z = 500$ m and correlate with the strong updrafts which may entrain warm air from the capping layer into the boundary layer.

During field experiment CASES-99, there were a lot of other instruments deployed. Figure 20 shows a 60 m main tower located at the center of our computational domain, downwind

of the large radial velocity blob seen in the lidar data. Vertical velocity components measured by 8 sonic anemometers along the tower are plotted in Fig. 21. The plot covers the period when volumes VOL13 to VOL16 were scanned. It shows a relatively strong updraft occurring around 19:42:50 UTC. The following downdraft occurred 90 seconds later is only very apparent near the top of the tower. It is certainly possible that the downdraft is even stronger above the tower top, but it cannot be said with certainty. Note that case AC1 covers from 19:42:28 to 19:45:28 UTC in time, while AC2 covers from 19:44:00 to 19:47:00. The general trend in the tower vertical velocity measurements seems to correlate with the retrievals shown in Fig. 18. That is, there is an updraft advecting away from the lidar, passing through the tower. Then, it is followed by a downdraft.

It is interesting to note that the downdraft observed in Fig. 18 resembles the "microburst" (Lester 1995), which is depicted as a strong downburst with a small length scale. Table 4 lists the features of a typical microburst and those of the retrieved structure described previously. The length scale of the retrieved downdraft is $1000 - 2000$ m, estimated from the region of high pressure fluctuations in Fig. 18. While the same downdraft is found in the retrieved flow fields for all four cases using observations VOL13-VOL17, it is not observed in the data retrieved from VOL12 or VOL18. This suggests that the downdraft life time is at least about 8 minutes, spanning from VOL13 to VOL17. The peak outflow velocity of the retrieved structure is about 6 m s^{-1}, smaller than $10 - 12$ m s^{-1} of a typical microburst. It appears that the retrieved downdraft has similar length scale and life time as a typical microburst, but with smaller strength in peak outflow velocity. The typical microburst is often induced by precipitation. Current downdraft retrieved from HRDL data measured in the afternoon is speculated to be a dry microburst because there was no precipitation observed during the lidar measurements. Wakimoto (1985) indicates that most dry microbursts occur in the afternoon. The term "microburst" usually refers to the small scale downdraft producing critical wind shear conditions. The retrieved downdraft may not belong to a category that poses a severe aviation hazard due to its weak strength.

Microburst detection usually tracks high radial velocity gradient regions as microburst signatures (May, 2001). For instance, the isosurface of high radial velocity in Fig. 2 signifies a microburst event. While an ideal microburst usually appears as a downburst accompanied by a circular vortex ring, the current downdraft is weak and the front boundary does not exhibit a clear arc shape. One possible explanation is that current HRDL data assimilation only uncovers a sector of a circular ring structure.

After data assimilation, many analyses are possible with the retrieved flow field information. For instance, 3D vortical structures can be revealed by displaying the negative pressure iso-surface. Figure 22 shows the iso-surface of negative pressure fluctuation $p/\rho_\circ = -5.0$ m^2 s^{-2}, with pressure contours and fluctuation velocity vectors shown in the two vertical planes at $x = 1575$ m and $y = -25$ m. The high pressure region indicates the downdraft and the velocity divergence can also be clearly identified near the ground in Fig. 22. The data are those retrieved at $t = 90$ s from case AC5 (the fine grid case). A big spanwise vortical structure is seen at the center of the computational domain close to $z = 500$ m. Another vortex at $(x,\ y) = (1500,\ -500)$ m touches the ground. Fluctuating velocity vectors in the two vertical planes at $y = 175$ m and $y = -575$ m are shown in Fig. 23, confirming that these low-pressure regions indicated by the arrows are indeed vortical motions. It is noteworthy that the locations of the vortices occur at heights where retrieved eddy viscosities, shown in Fig. 13, are local maxima.

The above observations are illustrated in Fig. 24. A downdraft creates strong high-speed outflow motion. The motion subsequently generates vortex A which resembles the vortex ring in a typical microburst, vortex B which precedes the outflow front, and wave-like motion between the vortices. Upward motion of vortex A could mix the warm air from the capping layer down into the boundary layer.

The adjoint retrieval of a wet microburst from radar data was performed by Xu et al. (2001) using a very simple two-dimensional model. To our knowledge, there has not yet been a four-dimensional data assimilation of microburst events. Vortical structures along with weak downdraft have not yet been reported in LES of ABL flows. Thus, 4D-Var is a promising tool for study of microscale ABL structures, and for detection of severe atmospheric structures.

6 Conclusions and Discussions

In this paper, a 4D-Var data assimilation model using an adjoint method is applied to high resolution Doppler lidar radial velocity data. Before assimilating actual lidar data, ITEs are used to evaluate the effects of buffer zones and boundary conditions. Results show that buffer zones enclosing lidar volume data help prevent inaccurate boundary conditions from affecting retrieval in the central region. With buffer zones employed and simplified boundary conditions, the 4D-Var model can yield good results. The current 4D-Var model treats the

initial fields and profiles of eddy viscosity and thermal diffusivity as control variables. The model is then applied to assimilate HRDL observations. Radial velocities regenerated from the retrieved flow fields agree well with the original data. Accuracy of retrieved data is assessed by a grid sensitivity test. It is found that the major source of errors in the 4D-Var lies in the cross-beam velocity component when data are scarce. A series of retrieval experiments generate several 3D wind and temperature fields in a convective boundary layer. A downdraft resembling a dry microburst is identified. The flow structure generates vortices and wave-like motions.

During the month of CASES-99 field experiments, several interesting phenomena were observed. For instance, Newsom and Banta (2003) and Blumen et al. (2001) analyzed a Kelvin-Helmholtz billow event in the nocturnal boundary layer. The huge amount of measurement data from CASES-99 offer great opportunities to study atmospheric structures. It also poses a big challenge to extract useful information from measurements. 4D-Var is extremely time-consuming and memory-demanding due to its complex 4D and nonlinear properties. Only relatively small grids are used in the data assimilation. Nevertheless, current application of 4D-Var techniques to HRDL observations demonstrates that 4D-Var can be a useful tool for the study of microscale atmospheric structures.

Acknowledgments:

This work is supported by the National Science Foundation (Grant number ATM-9874925), monitored by Dr. Roddy R. Rogers. The National Center for Atmospheric Research, the National Partnership for Advanced Computational Infrastructure, and the National Center for Super-computing Applications, sponsored by the National Science Foundation, are acknowledged for the computing time used in this research. Funding for field measurements was provided by the Army Research Office, the Center for Geosciences/Atmospheric Research at Colorado State University, and the National Science Foundation (Grant number ATM-9908453). The authors are indebted to the organizers of the CASES-99 field program and to the members of the Optical Remote Sensing Division at NOAA/ETL.

References

[1] Banta, R. M., R. K. Newsom, J. K. Lundquist, Y. L. Pichugina, R. L. Coulter, and L. D. Mahrt, 2002: Nocturnal low-level jet characteristics over Kansas during CASES-99. *Boundary-Layer Meteor. 105*, 221–252.

[2] Blumen, W., R. M. Banta, S. P. Burns, D. C. Fritts, R. K. Newsom, G. S. Poulos, and J. Sun, 2001: Turbulent statistics of a Kelvin-Helmholtz billow event observed in the nighttime boundary layer during the CASES-99 field program. *Dynam. Atmos. Oceans 34*(2-4), 189–204.

[3] Chai, T. and C.-L. Lin, 2002: Optimization of turbulent viscosity and diffusivity in adjoint recovery of atmospheric boundary layer flow structures. Submitted to *Multiscale Modeling and simulation*.

[4] Cooper, D., W. Eichinger, R. Ecke, J. Kao, J. Reisner, and L. Tellier, 1997: Initial investigation of microscale cellular convection in an equatorial marine atmospheric boundary layer revealed by lidar. *Geophys. Res. Lett. 24*, 45–48.

[5] Daescu, D., G. R. Carmichael, and A. Sandu, 2000: Adjoint implementation of Rosenbrock methods applied to variational data assimilation problems. *J. Comput. Physics. 165*(2), 496–510.

[6] Eichinger, W., D. Cooper, F. Archuletta, D. Hof, D. Holtkamp, R. Karl Jr., C. Quick, and J. Tiee 1994: Development of a scanning, solar-blind, water raman lidar. *Applied Optics 33*(18), 3923–3932.

[7] Ezer, T. and G.L. Mellor, 2000: Sensitivity studies with the north Atlantic sigma coordinate Princeton Ocean Model. *Dynam. Atmos. Oceans 32*, 185–208.

[8] Gavart, M., P. De Mey and G. Canizux, 1999: Assimilation of satellite altimeter data in a primitive-equation model of the Azores-Madeira region. *Dynam. Atmos. Oceans 29*, 217–254.

[9] Gerard E. and R. W. Saunders, 1999: Four-dimensional variational assimilation of special sensor micorwave/imager total column water vapour in the ECMWF model. *Q. J. R. Meteorol. Soc. 125*, 3077–3101.

[10] Glendening, J., 1996: Lineal eddy features under strong shear conditions. *J. Atmos. Sci. 53*, 3430–3449.

[11] Grund, C. J., R. M. Banta, J. L. George, J. N. Howell, M. J. Post, R. A. Richter, and A. M. Weickmann, 2001: High-Resolution Doppler Lidar for boundary-layer and cloud research. *J. Atmos. Oceanic Technol. 18*, 376–393.

[12] Jacobson, M. Z. 1999: *Fundamentals of atmospheric modeling*. New York: Cambridge University Press.

[13] Khanna, S. and J. Brasseur, 1998: Three-dimensional buoyancy- and shear-induced local structure of the atmospheric boundary layer. *J. Atmos. Sci. 55*, 710–743.

[14] Lenschow, D. H., Wyngaard, J. C., and W. T. Pennell, 1980: Mean-field and second-moment budgets in a baroclinic, convective boundary layer. *J. Atmos. Sci. 37*, 1313–1326.

[15] Lester, P., 1995: *Aviation weather*. Englewood, Colorado: Jeppesen Sanderson, Inc.

[16] Lin, C.-L., J. C. McWilliams, C.-H. Moeng, and P. P. Sullivan, 1996: Coherent structures and dynamics in a neutrally stratified planetary boundary layer flow. *Phys. Fluids 8*(10), 2626–2639.

[17] Lin, C.-L., 2000: Local pressure-transport structure in a convective atmospheric boundary layer. *Phys. Fluids 12*(5), 1112–1128.

[18] Lin, C.-L., T. Chai, and J. Sun, 2001: Retrieval of flow structures in a convective boundary layer using an ajoint model: identical twin experiments and coherent structures in the convective planetary boundary layer, *J. Atmos. Sci. 58*(13), 1767–1783.

[19] Lin, C.-L. and T. Chai, 2002: On smoothness constraints for four-dimensional data assimilation. *J. Comp. Physics.. 181*, 430–453.

[20] Liu, D. C. and J. Norcedal, 1989: On the limited memory BFGS method for large scale optimization. *Math. Programming. 45*(3), 503–528.

[21] Long, R. B. and W. C. Thacker, 1989: Data assimilation into a numerical equatorial ocean model. Part 2: Assimilation experiments. *Dyn. Atmos. Oceans. 13*, 413–439.

[22] May, P. T., 2001: Mesocyclone and microburst signature distortion with dual PRT radars. *J. Atmos. Ocean. Tech 18*(7), 1229–1233.

[23] Moeng, C.-H., 1984: A large-eddy-simulation model for the study of planetary boundary-layer turbulence. *J. Atmos. Sci. 41*, 2052–2062.

[24] Moeng, C.-H. and P. P. Sullivan, 1994: A comparison of shear- and buoyancy-driven planetary boundary layer flows. *J. Atmos. Sci. 51*, 999–1022.

[25] Newsom, R. K. and R. M. Banta, 2003: Shear flow instability in the stable nocturnal boundary layer as observed by Doppler lidar during CASES-99. *J. Atmos. Sci. 60*, 16–33.

[26] Sullivan, P. P, J. C. McWilliams, and C.-H. Moeng, 1994: A subgrid-scale model for large-eddy simulation of planetary boundary-layer flows. *Boundary-Layer Meteorol. 71*, 247–276.

[27] Sun, J., D. W. Flicker, and D. K. Lilly, 1991: Recovery of three-dimensional wind and temperature fields from simulated single-Doppler radar data. *J. Atmos. Sci. 48*, 876–890.

[28] Sun, J. and A. Crook, 1996: Comparison of thermodynamic retrieval by the adjoint method with the traditional retrieval method. *Mon. Wea. Rev. 124*, 308–324.

[29] Sun, J., and A. Crook, 1998: Dynamical and microphysical retrieval from Doppler radar observations using a cloud model and its adjoint. Part II: Retrieval experiments of an observed Florida Convective Storm. *J. Atmos. Sci. 55*, 835–852.

[30] Wakimoto, R. M., 1985: Forcasting dry microburst activity over the high-plains. *Mon. Wea. Rev. 113*(7), 1131–1143.

[31] Weckwerth, T. M., C. J. Grund, and S. D. Mayor, 1997: Linearly-organized coherent structures in the surface layer. *12th Symposium on Boundary Layers and Turbulence*, Vancouver, British Columbia, Canada, 22.

[32] Wulfmeyer, V., M. Randall, W. A. Brewer, and R. M. Hardesty, 2000: 2 μm Doppler lidar transmitter with high frequency stability and low chirp. *Opt. Lett. 25*, 1228–1230.

[33] Xu, Q., H. Gu, and C. Qiu, 2001: Simple adjoint retrievals of wet-microburst winds and gust-front winds from single-Doppler Radar data. *J. Applied Meteorology 40*, 1485–1499.

Table 1: ITE Descriptions. BC, boundary conditions; restrictions, restriction on ranges of elevation and azimuth angles for observations.

Case	Descriptions
IT1	Dirichlet BC, big domain,restrictions, 50 iterations
IT2	Inflow/outflow BC, big domain,restrictions, 50 iterations
IT3	Dirichlet BC, small domain, restrictions, 50 iterations
IT4	Inflow/outflow BC, small domain, restrictions, 50 iterations
IT5	Dirichlet BC, big domain, no restrictions, 50 iterations
IT6	Radial velocity with 20 observational errors, others same as IT1
IT7	Radial velocity with -0.1 to 0.1 m s^{-1}, others same as IT2

Table 2: Correlation coefficients (σ) and RMS errors (ϵ) of ITEs at 50 iterations, averaged throughout the scan volume where $z < 400$ m.

Case	σ_U	σ_V	σ_W	σ_θ	ϵ_U	ϵ_V	ϵ_W	ϵ_θ
IT1	0.885	0.898	0.868	0.712	0.465	0.468	0.526	0.225
IT2	0.886	0.899	0.882	0.745	0.470	0.466	0.491	0.197
IT3	0.869	0.871	0.829	0.519	0.562	0.578	0.627	0.286
IT4	0.875	0.875	0.855	0.543	0.546	0.563	0.580	0.254
IT5	0.863	0.889	0.868	0.649	0.513	0.512	0.517	0.237
IT6	0.875	0.894	0.868	0.723	0.483	0.478	0.524	0.212
IT7	0.887	0.900	0.883	0.745	0.469	0.464	0.490	0.198

Table 3: Descriptions and results of cases using HRDL data. NTER, number of iterations

Case	Inputs	$NX \times NY \times NZ$	NTER for $\Delta \leq 0.2$ m s^{-1}
AC1	VOL 13, VOL 14	$48 \times 48 \times 25$	83
AC2	VOL 14, VOL 15	$48 \times 48 \times 25$	83
AC3	VOL 15, VOL 16	$48 \times 48 \times 25$	99
AC4	VOL 16, VOL 17	$48 \times 48 \times 25$	90
AC5	VOL 15, VOL 16	$48 \times 48 \times 50$	146

Table 4: Comparison between typical microbursts (Lester 1995) and the retrieved downburst.

Features	Typical microbursts	Downburst in the retrieval
Horizontal dimensions	4,000 m or less	$1,000 - 2,000$ m
Life time	$5 - 30$ minutes	$\sim$ 8 minutes
Peak outflow speed	$10 - 12$ m s^{-1}	~ 6 m s^{-1}
Formation	Mostly induced by prescipation	Resulted from unstable CBL in the afternoon

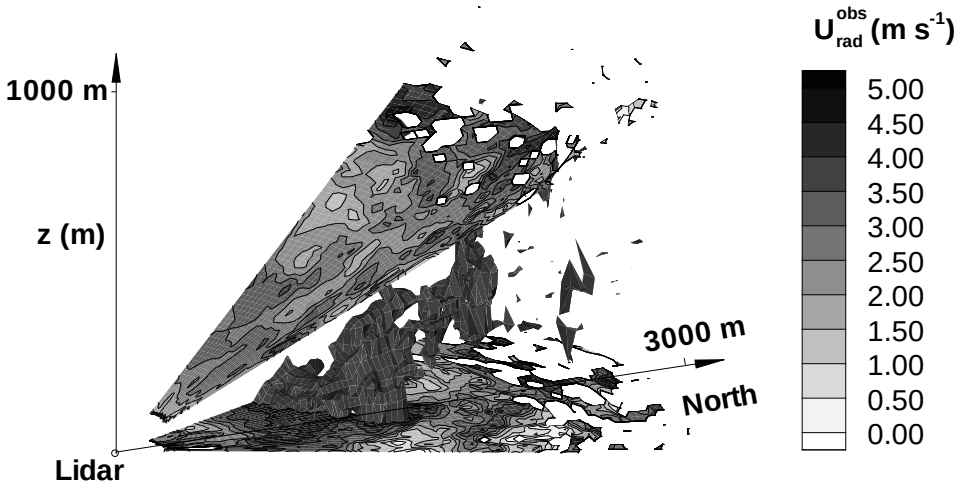

Figure 1: Illustration of a typical scan volume, VOL15. Radial velocity contours at 1° and 19° elevation angles and an iso-surface of $U_{rad}^{obs} = 5$ m s^{-1} are shown. Bad data have been removed.

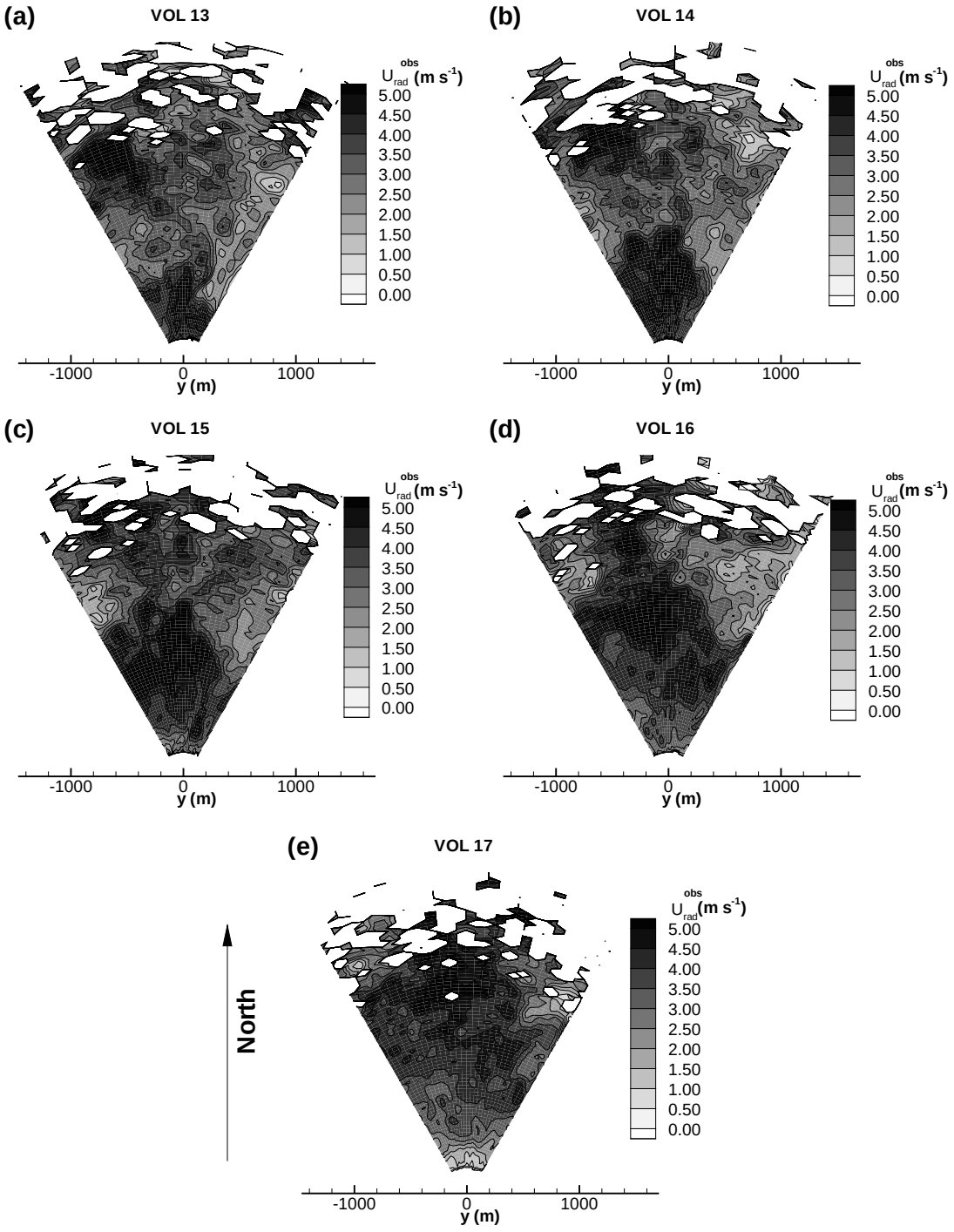

Figure 2: Radial velocity contours at 5° elevation from observations of VOL13 to VOL17 (a)∼(e).

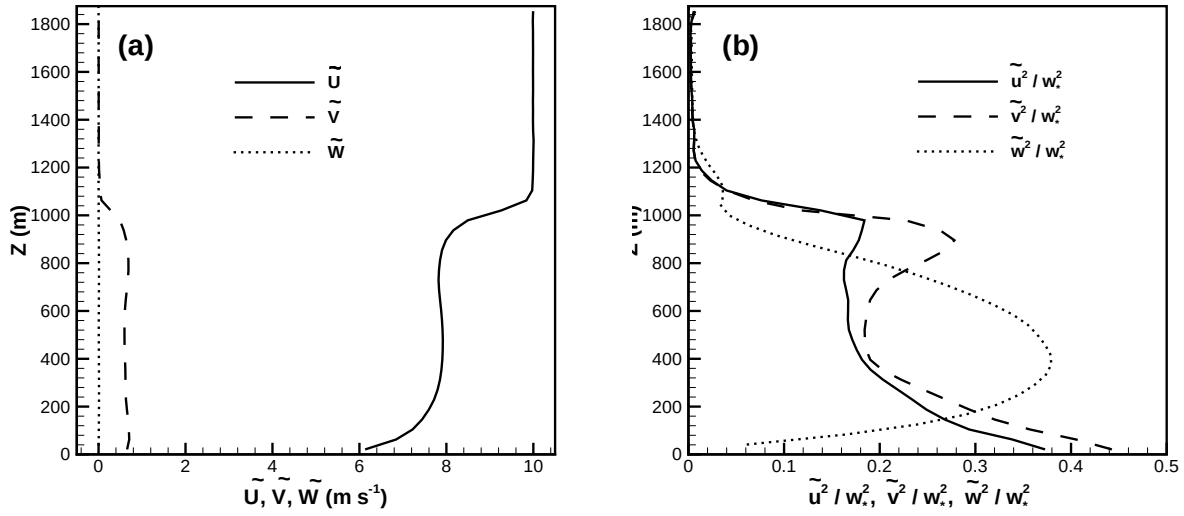

Figure 3: Vertical distributions of (a) mean velocity and (b) normalized velocity variance. "< >" denotes averaging over time and $x - y$ plane. w_* is the free-convection velocity scale, and $w_* = 2.0$ m s^{-1}.

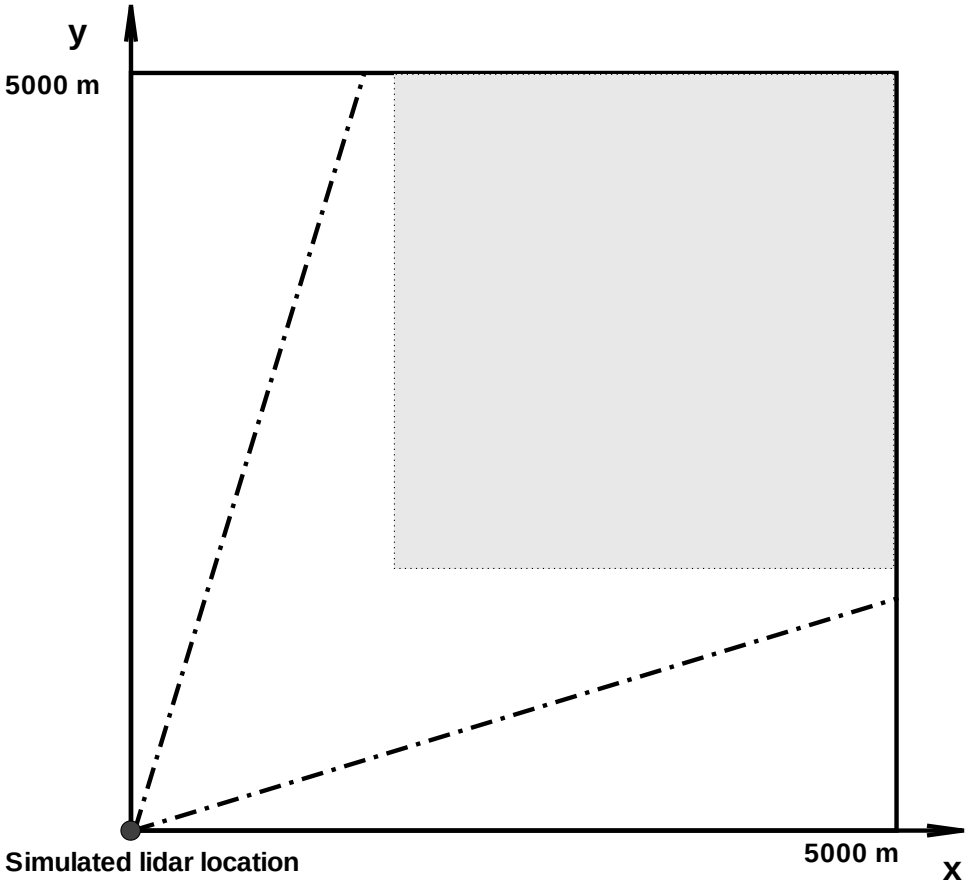

Figure 4: Illustration of different computational domains: the small domain in gray is used for cases IT3 and IT4. The big region covering the scan volume is used for all the other ITEs.

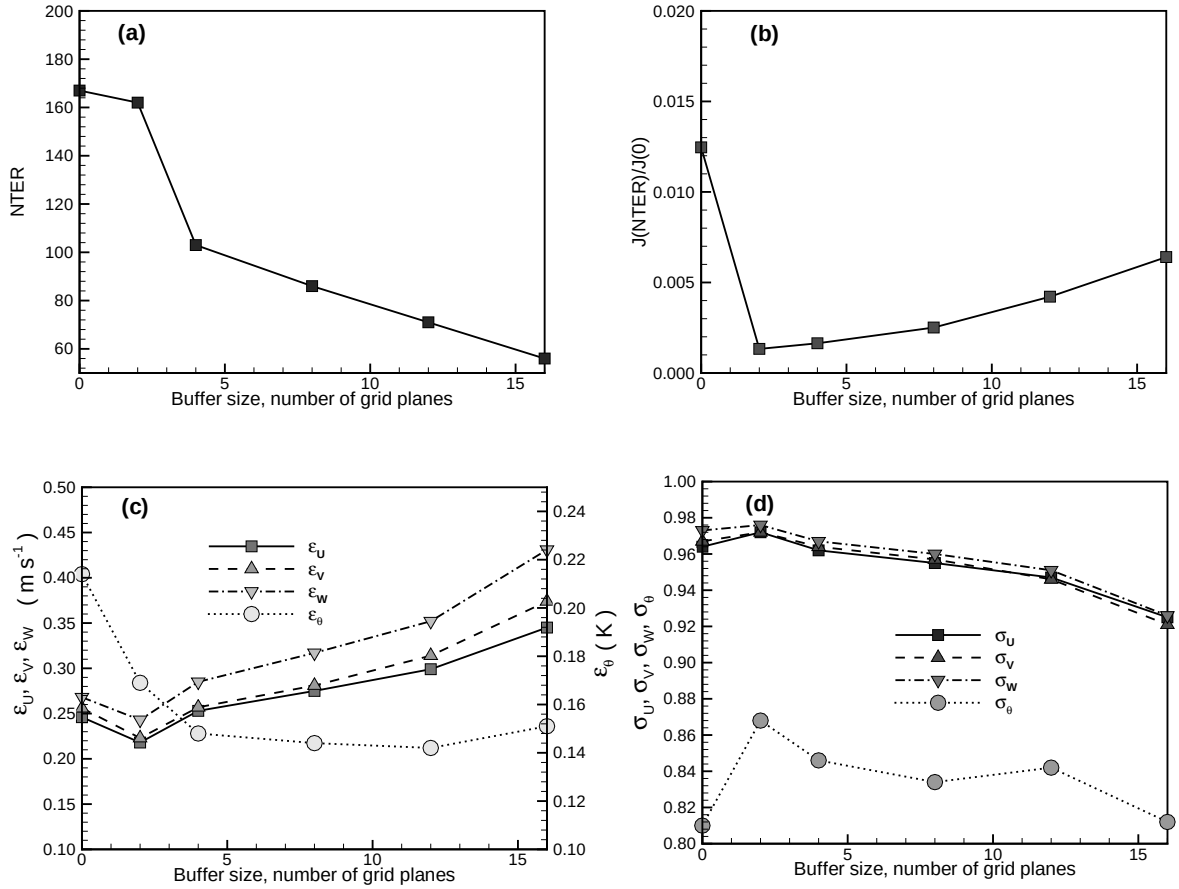

Figure 5: The number of required iterations (NTER), normalized cost function, RMS errors, and correlation coefficients versus buffer size at four lateral boundaries. Errors and correlation coefficients are calculated using the data in a $16 \times 16 \times 20$ center lower region.

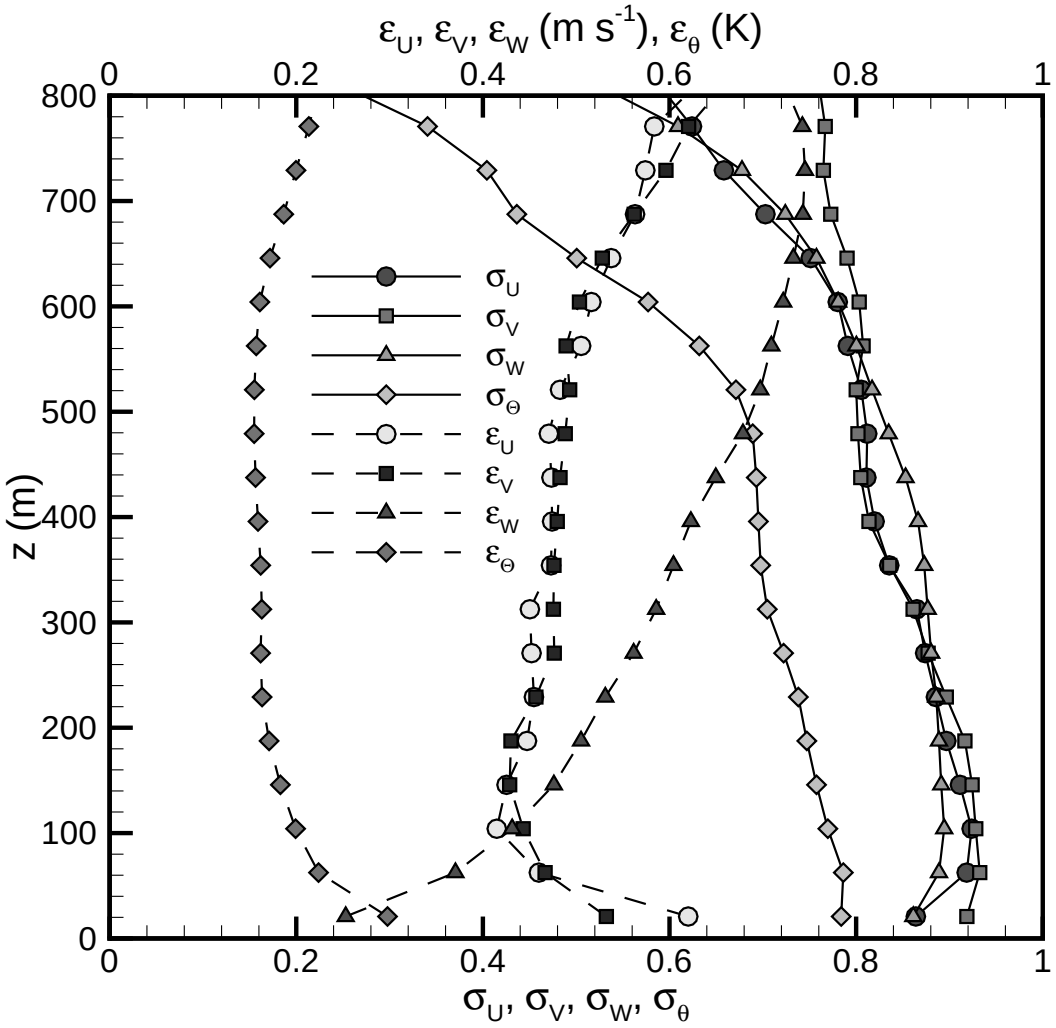

Figure 6: Vertical distributions of correlation coefficients σ and RMS errors ϵ for case IT2 at $t = 150$ s.

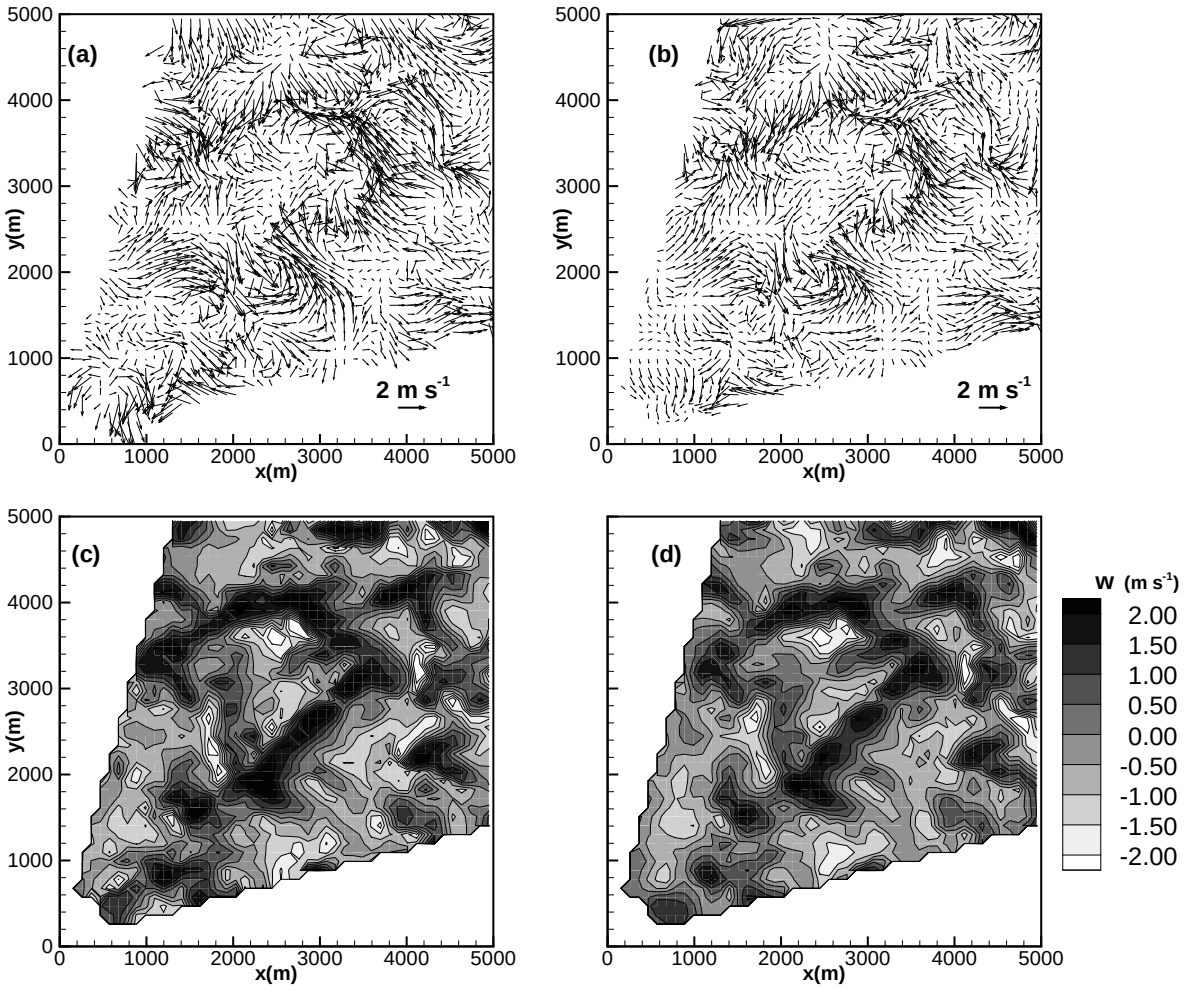

Figure 7: Comparison of retrieved velocity fluctuations from IT2 with exact ones generating the observations, at $z = 229$ m, $t = 150$ s. (a) the exact (u, v); (b)the retrieved (u, v). (c) contours of the exact w_o; (d) contours of the retrieved w. (c) and (d) use the same contour levels.

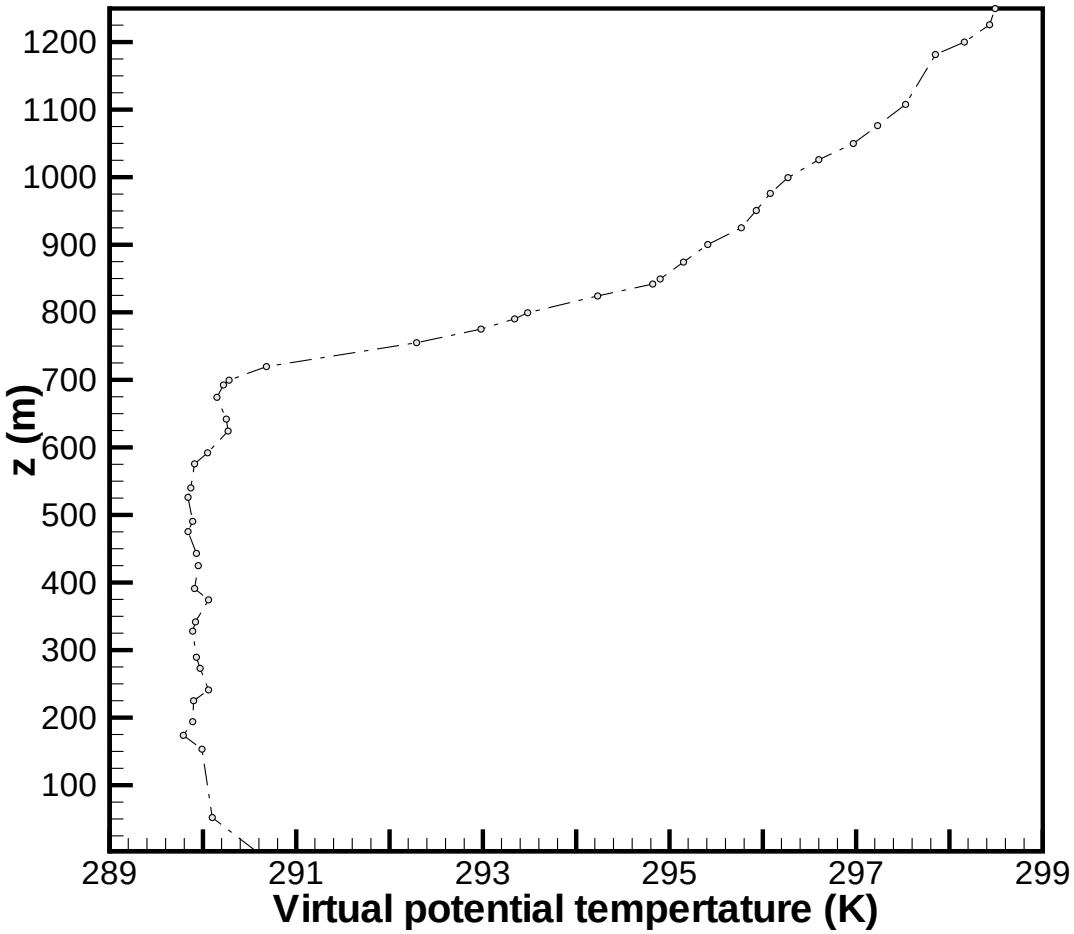

Figure 8: Mean virtual potential temperature profile calculated from sounding data.

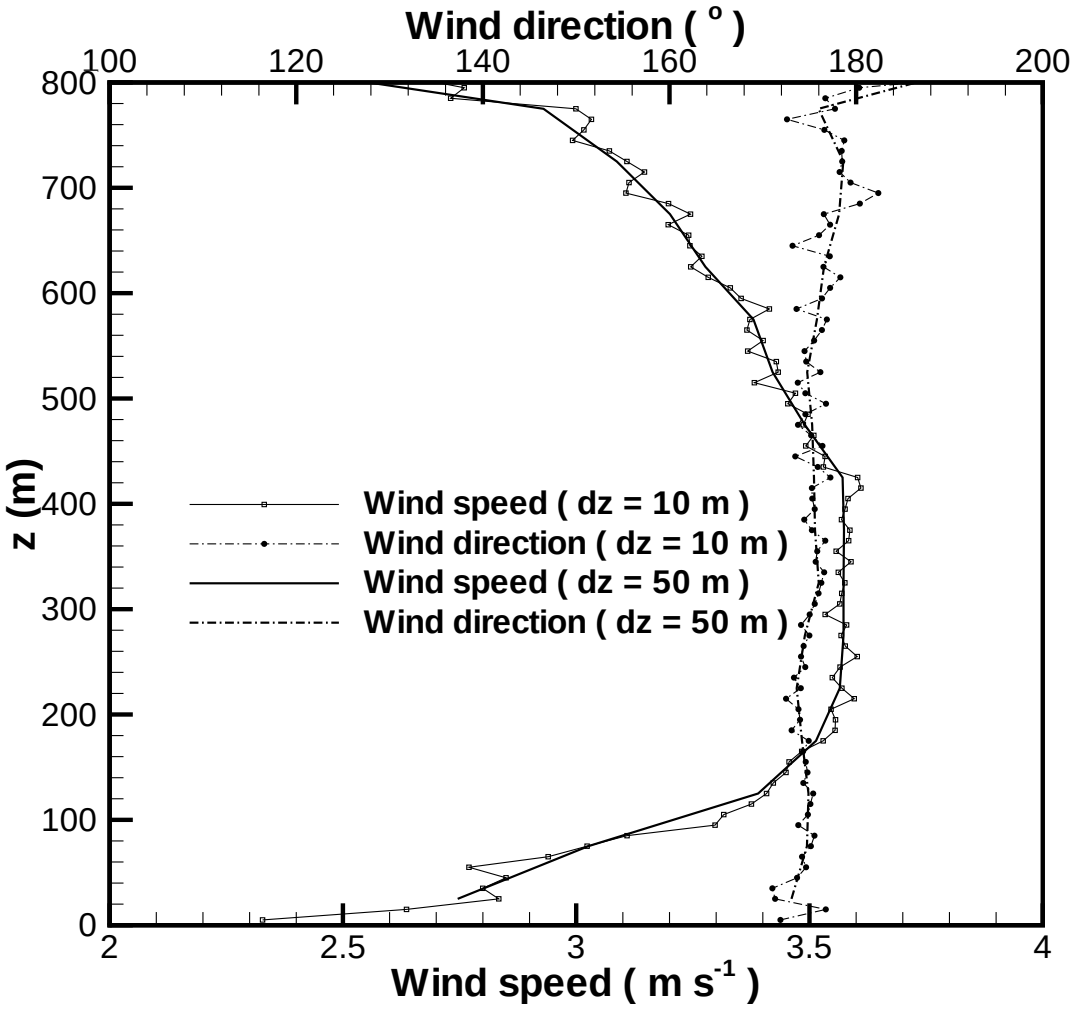

Figure 9: Mean wind profiles approximated from the bin method.

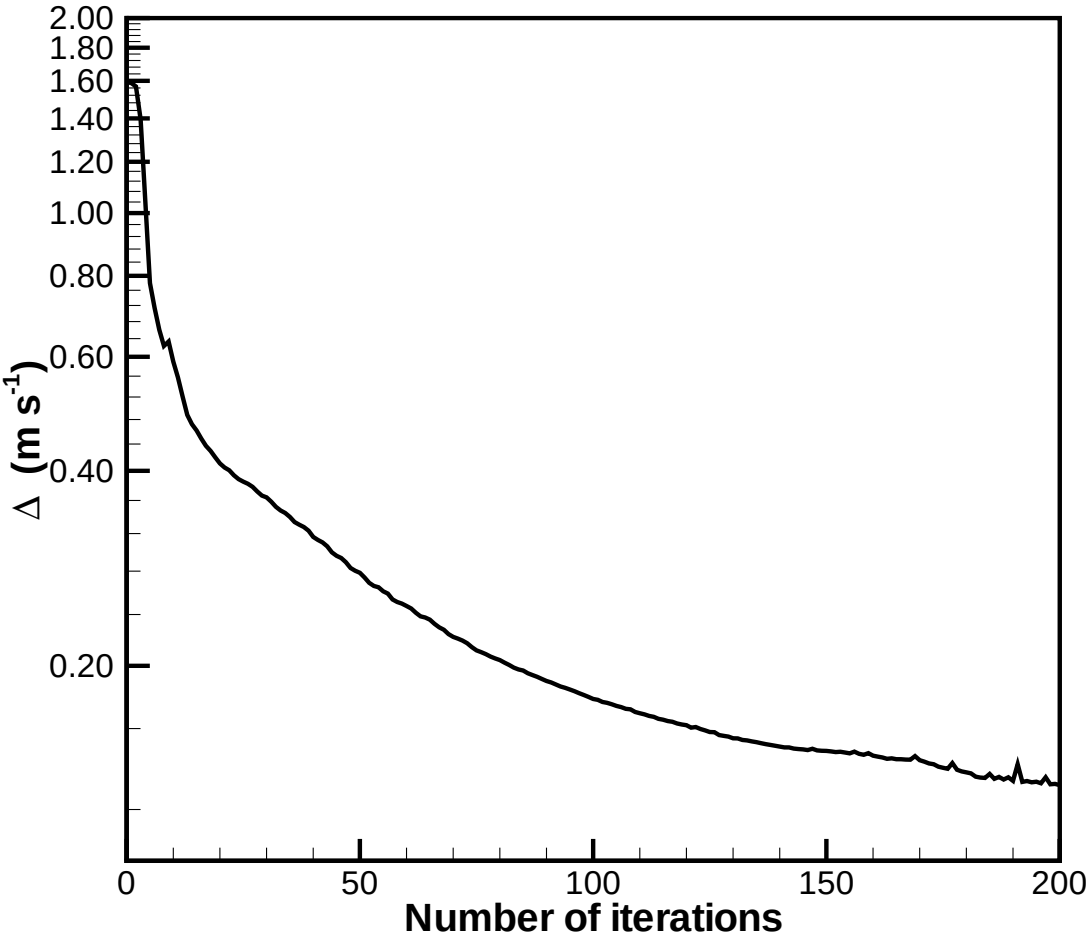

Figure 10: Variation of radial velocity misfit Δ versus number of iterations for case AC2.

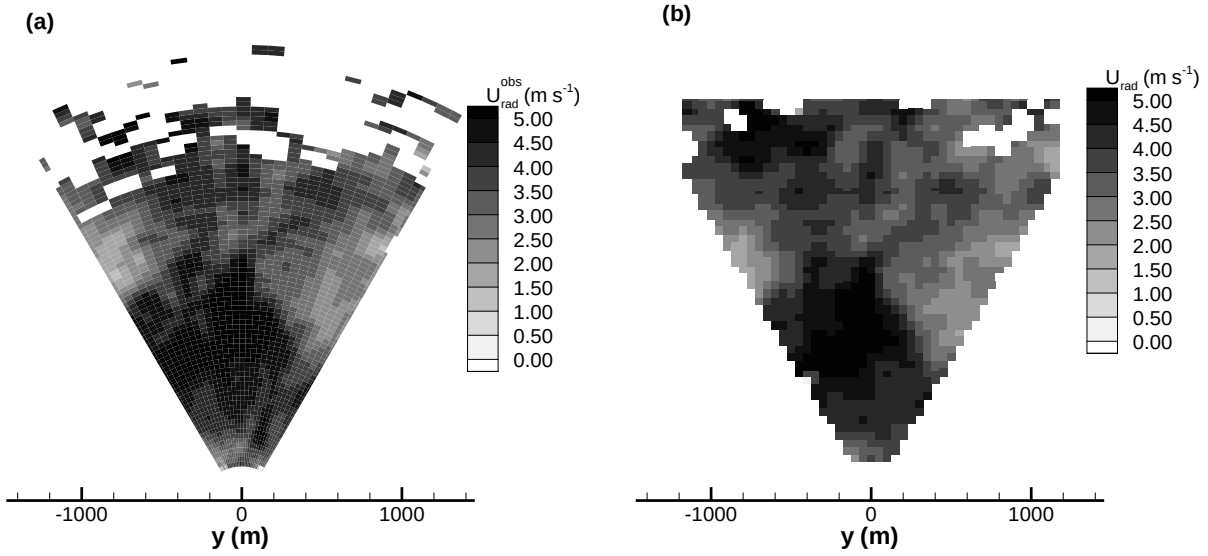

Figure 11: Comparison of would-be radial velocities with HRDL observations. The scan plane at 5° elevation in VOL15 and the corresponding would-be radial velocities calculated from case AC2 are shown. (a) HRDL observations; (b) would-be radial velocities.

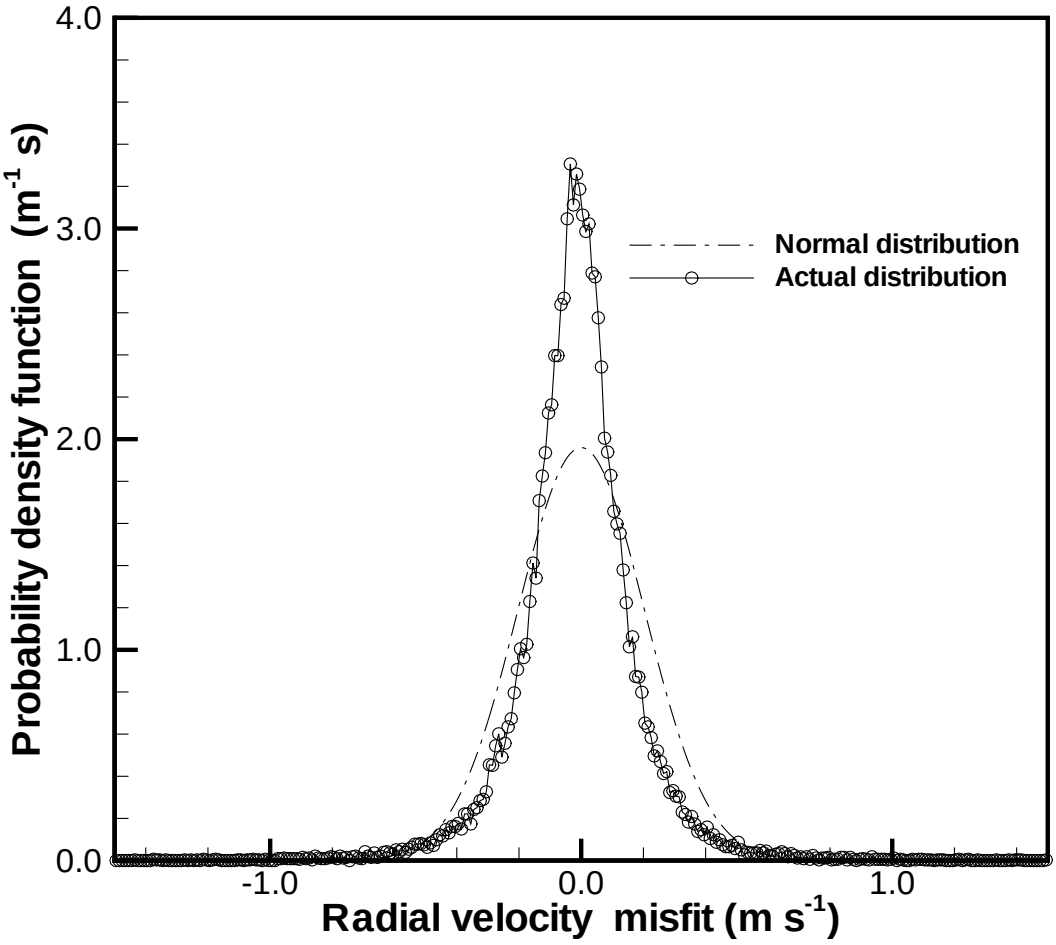

Figure 12: Distribution of radial velocity misfits for case AC2. A Normal distribution with the same mean and standard deviation as case AC2 is also shown for comparison.

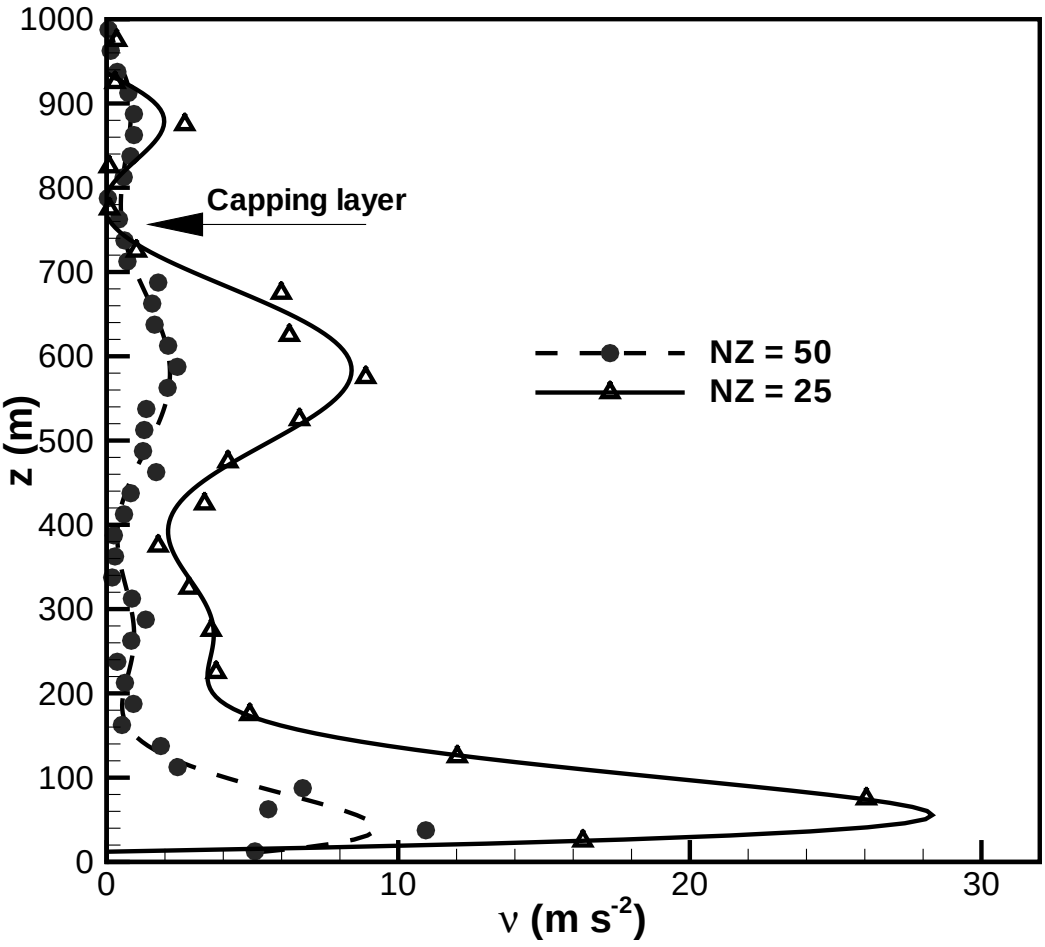

Figure 13: Comparison of estimated $\nu(z)$ using different vertical resolutions.

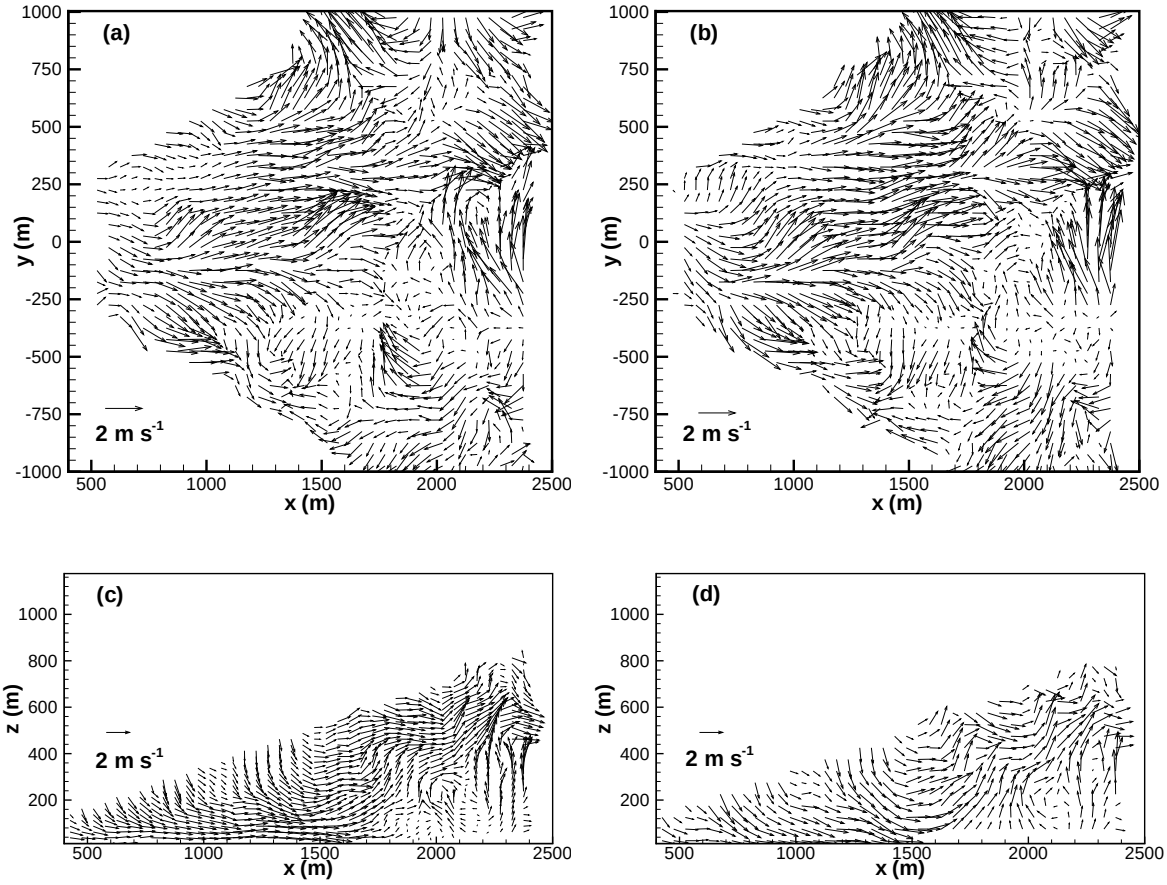

Figure 14: Comparison of retrieved flow fields from: (a) and (c), case AC5; (b) and (d), case AC3. Fluctuating velocity components are shown at: (a) and (b), z=175 m; (c) and (d), y=0 m

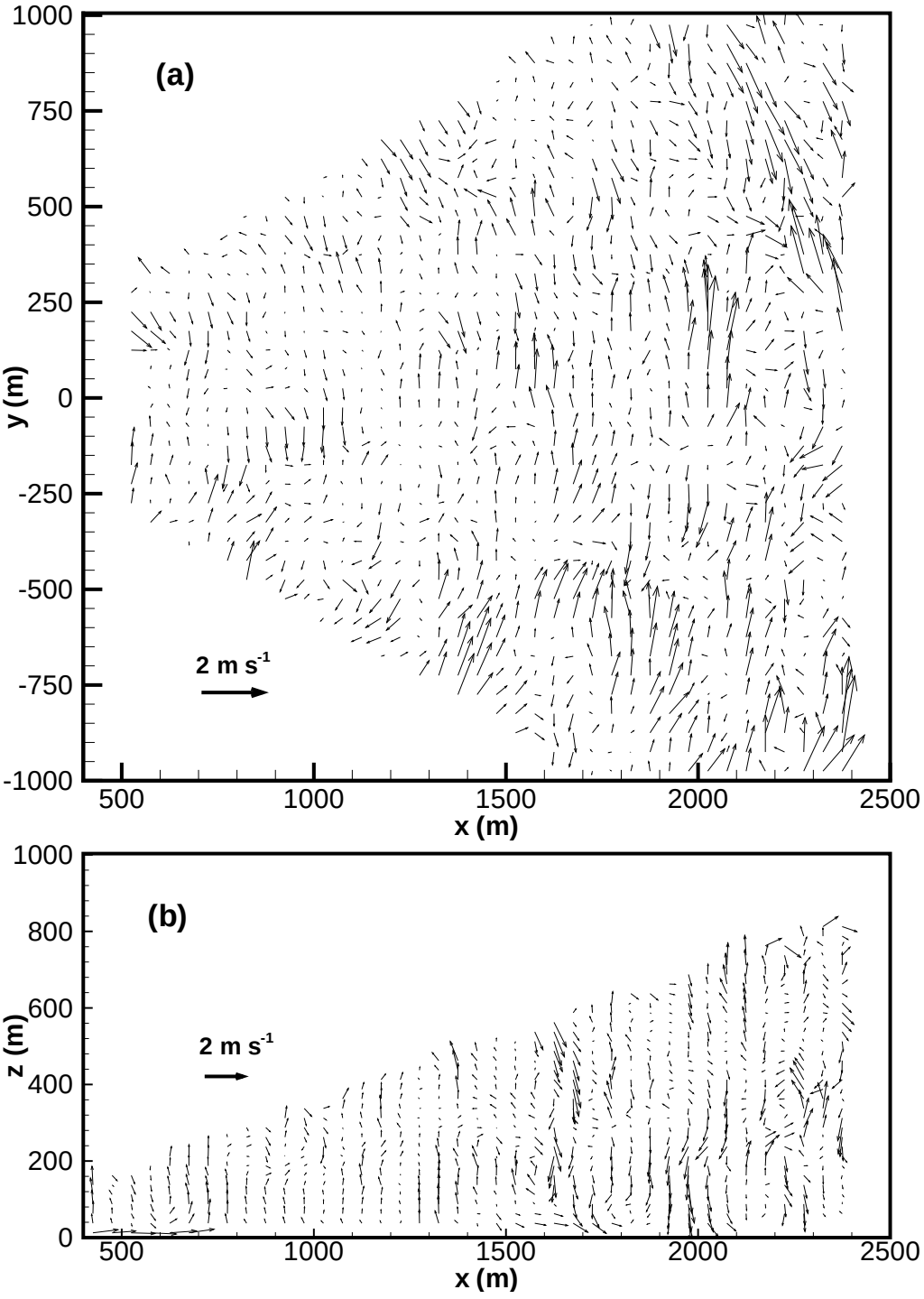

Figure 15: Difference between velocity vectors retrieved from coarse grid case AC3 and fine grid case AC5. (a) z=175 m; (b) y=0 m.

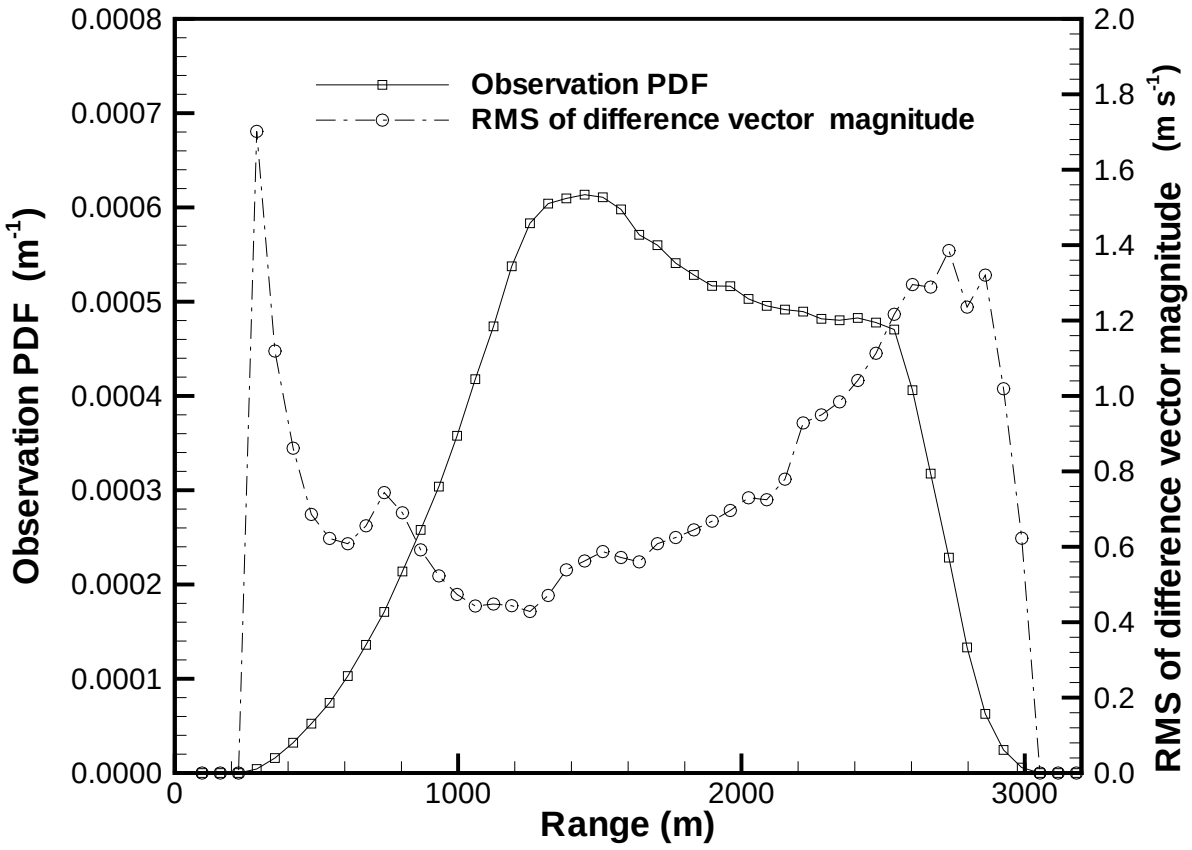

Figure 16: Observation PDF and RMS difference between velocity vectors retrieved from cases AC3 and AC5.

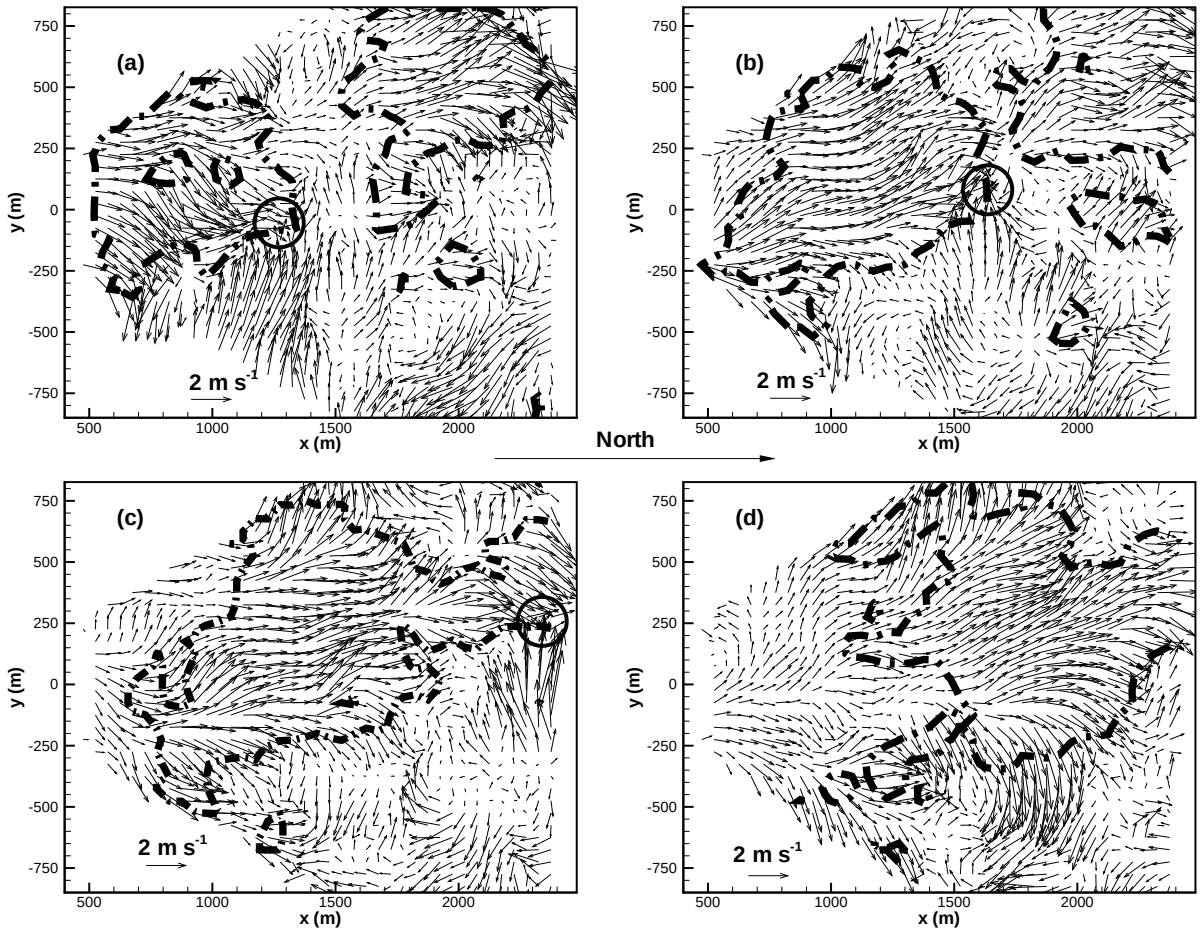

Figure 17: Instantaneous fluctuating velocity fields at $z = 175$ m for cases AC1-AC4 (a-d). Dot-dashed lines are the contour lines of $U_{rad} = 4.0$ m s^{-1}.

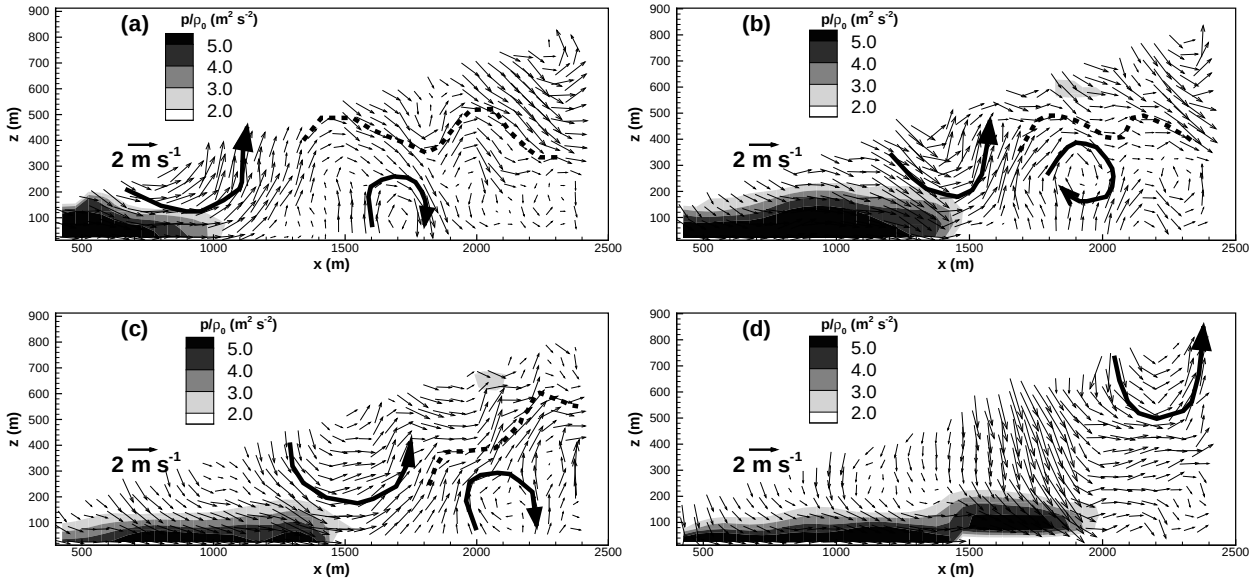

Figure 18: Instantaneous fluctuating velocity fields in the $y = 0$ vertical plane for cases AC1-AC4 (a-d). Fluctuating pressure contours are shown to indicate the downburst.

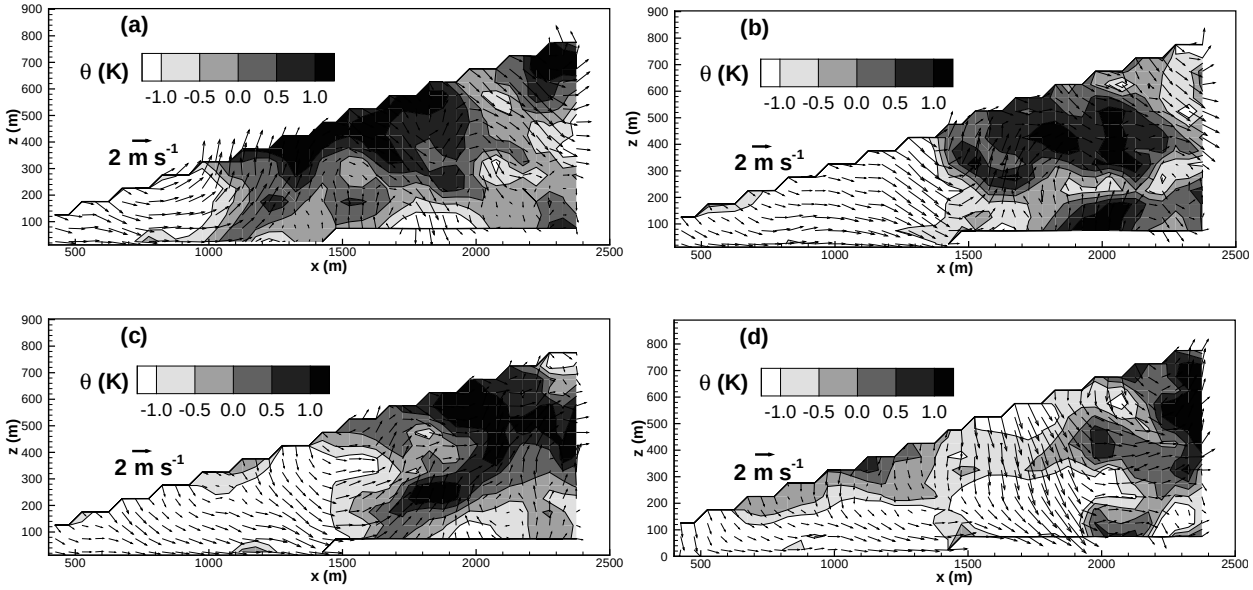

Figure 19: Fluctuating temperature contours in the $y = 0$ vertical plane for cases AC1-AC4 (a-d). Instantaneous fluctuation velocity fields are also shown.

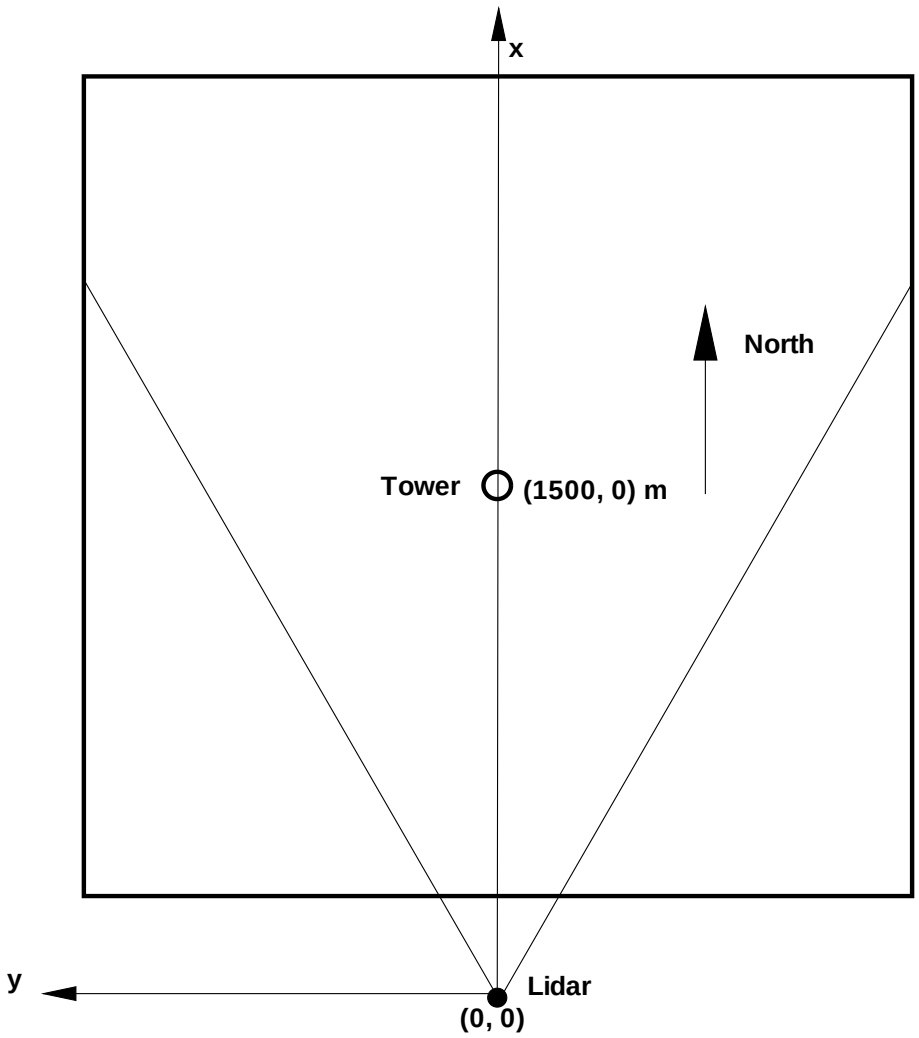

Figure 20: Location of the 60 m main tower in the current computational domain.

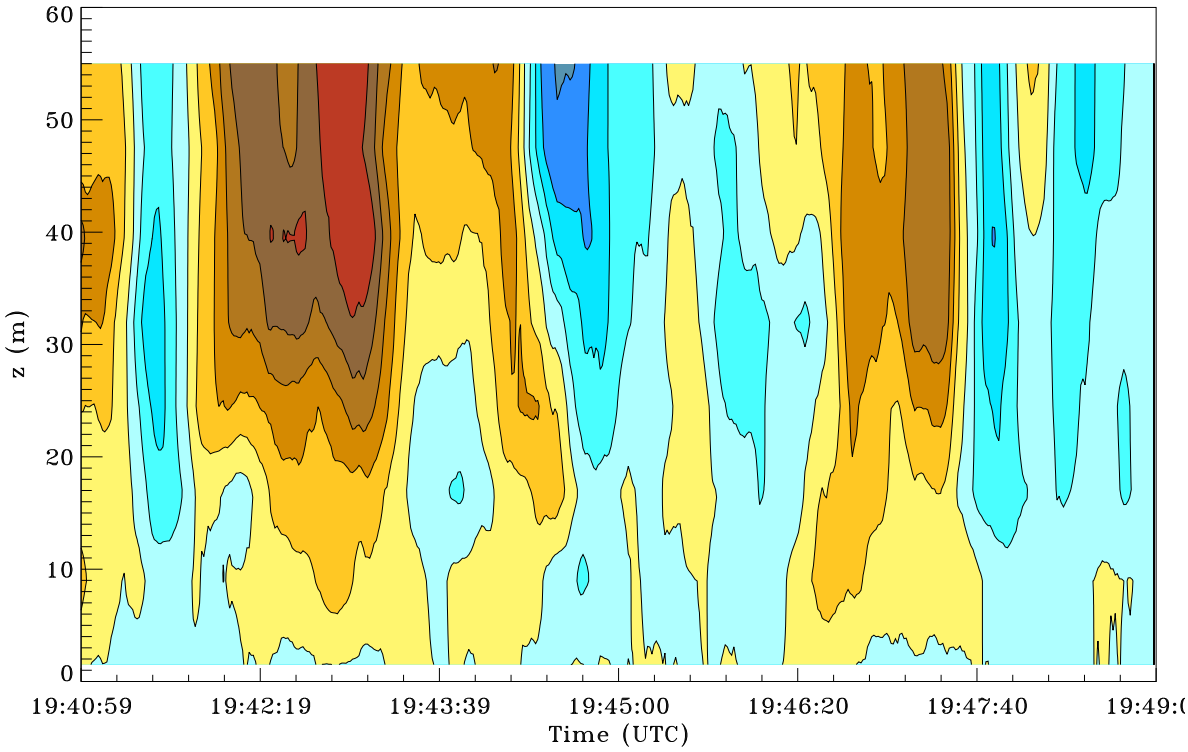

Figure 21: Vertical velocity measured by sonic anemometers along the 60 m main tower. The scale runs from -2.5 m s^{-1} (blue) to 2.5 m s^{-1} (red).

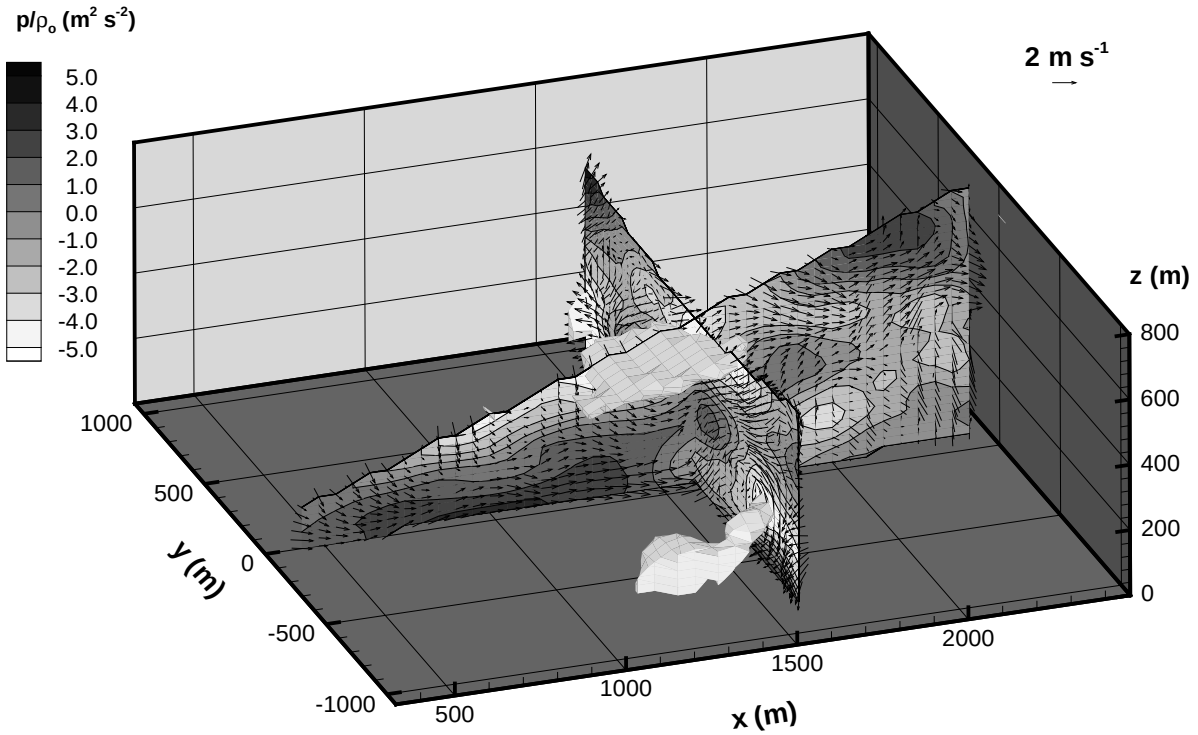

Figure 22: Instantaneous flow field 3D structures from case AC3 at $t = 90$ s. Iso-surfaces of fluctuating pressure $p/\rho_\circ = -5$ m^2 s^{-2}, fluctuating velocity vectors, and fluctuating pressure contours in vertical plane at $x = 1575$ m and $y = -25$ m are shown.

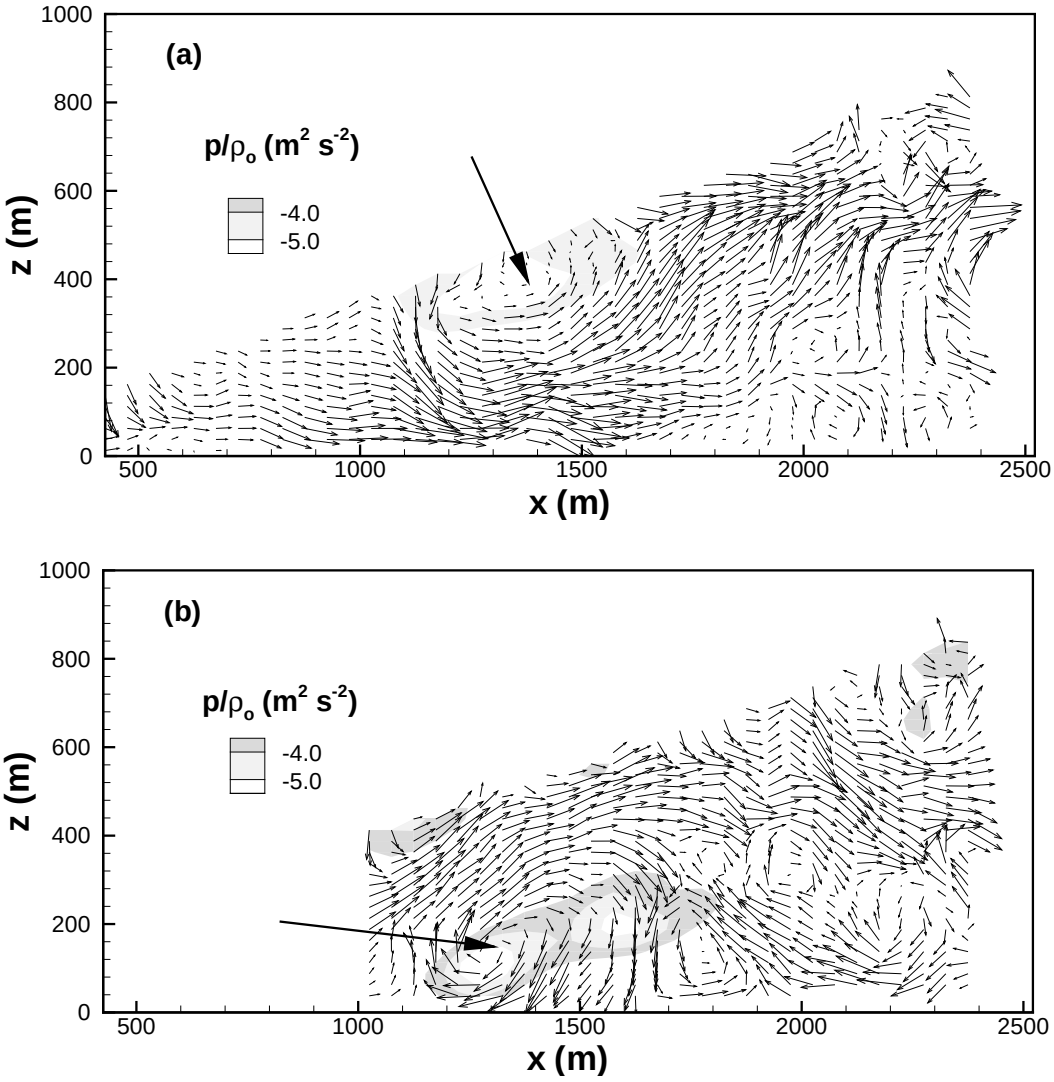

Figure 23: Fluctuating velocity vectors retrieved from case AC5 in vertical planes: (a) y=175 m; (b) y=-575 m.

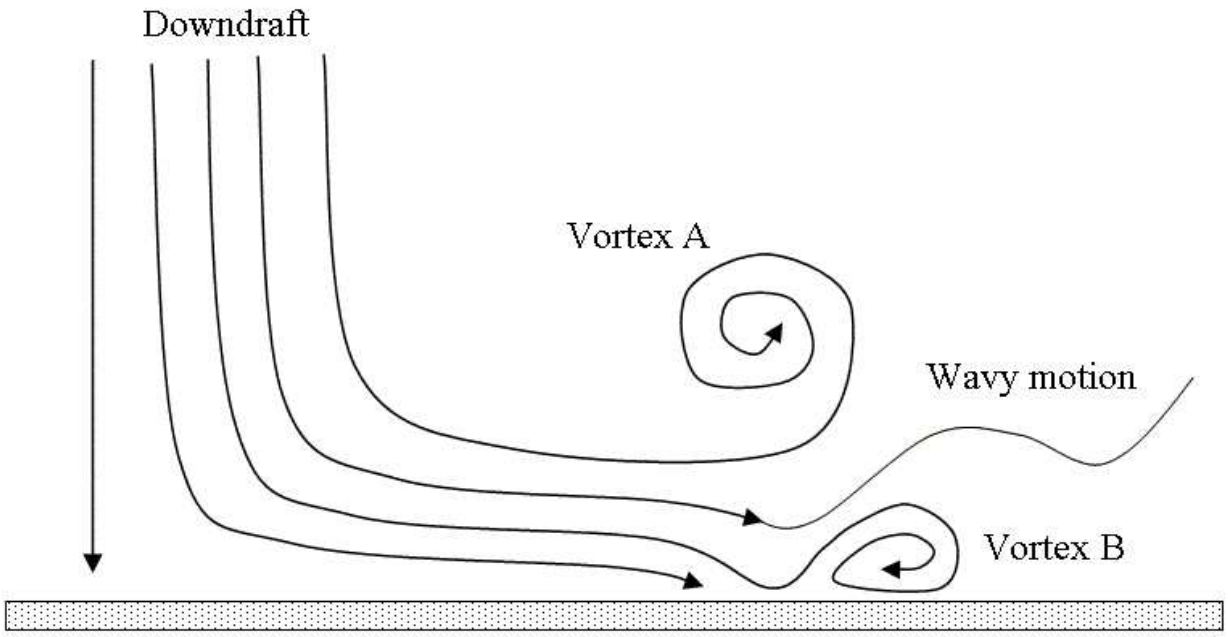

Figure 24: Recovered flow structure schematic.